



In vivo Estimation of Axonal Morphology From Magnetic Resonance Imaging and Electroencephalography Data

Rita Oliveira*, Andria Pelentritou, Giulia Di Domenicantonio, Marzia De Lucia and Antoine Lutti*

Laboratory for Research in Neuroimaging, Department of Clinical Neuroscience, Lausanne University Hospital and University of Lausanne, Lausanne, Switzerland

OPEN ACCESS

Edited by:

Andrada Ianus,
Champalimaud Foundation, Portugal

Reviewed by:

Maryam Afzali,
Cardiff University, United Kingdom
Eirini Messaritaki,
Cardiff University, United Kingdom

*Correspondence:

Rita Oliveira
Ana.Veiga-De-Oliveira@chuv.ch
Antoine Lutti
Antoine.Lutti@chuv.ch

Specialty section:

This article was submitted to
Brain Imaging Methods,
a section of the journal
Frontiers in Neuroscience

Received: 11 February 2022

Accepted: 24 March 2022

Published: 21 April 2022

Citation:

Oliveira R, Pelentritou A,
Di Domenicantonio G, De Lucia M
and Lutti A (2022) *In vivo* Estimation
of Axonal Morphology From Magnetic
Resonance Imaging
and Electroencephalography Data.
Front. Neurosci. 16:874023.
doi: 10.3389/fnins.2022.874023

Purpose: We present a novel approach that allows the estimation of morphological features of axonal fibers from data acquired *in vivo* in humans. This approach allows the assessment of white matter microscopic properties non-invasively with improved specificity.

Theory: The proposed approach is based on a biophysical model of Magnetic Resonance Imaging (MRI) data and of axonal conduction velocity estimates obtained with Electroencephalography (EEG). In a white matter tract of interest, these data depend on (1) the distribution of axonal radius [$P(r)$] and (2) the g-ratio of the individual axons that compose this tract [$g(r)$]. $P(r)$ is assumed to follow a Gamma distribution with mode and scale parameters, M and θ , and $g(r)$ is described by a power law with parameters α and β .

Methods: MRI and EEG data were recorded from 14 healthy volunteers. MRI data were collected with a 3T scanner. MRI-measured g-ratio maps were computed and sampled along the visual transcallosal tract. EEG data were recorded using a 128-lead system with a visual Poffenberg paradigm. The interhemispheric transfer time and axonal conduction velocity were computed from the EEG current density at the group level. Using the MRI and EEG measures and the proposed model, we estimated morphological properties of axons in the visual transcallosal tract.

Results: The estimated interhemispheric transfer time was 11.72 ± 2.87 ms, leading to an average conduction velocity across subjects of 13.22 ± 1.18 m/s. Out of the 4 free parameters of the proposed model, we estimated θ – the width of the right tail of the axonal radius distribution – and β – the scaling factor of the axonal g-ratio, a measure of fiber myelination. Across subjects, the parameter θ was 0.40 ± 0.07 μm and the parameter β was 0.67 ± 0.02 $\mu\text{m}^{-\alpha}$.

Conclusion: The estimates of axonal radius and myelination are consistent with histological findings, illustrating the feasibility of this approach. The proposed method allows the measurement of the distribution of axonal radius and myelination within a white matter tract, opening new avenues for the combined study of brain structure and function, and for *in vivo* histological studies of the human brain.

Keywords: MRI, EEG, axonal morphology, IHTT, *in vivo* histology

INTRODUCTION

The characterization of microscopic brain changes *in vivo* in clinical populations is essential to the understanding of brain disease. Magnetic Resonance Imaging (MRI) is non-invasive and the primary technique for the assessment of brain structure *in vivo* (Weiskopf et al., 2015; Kiselev and Novikov, 2018). MRI is sensitive to a large array of microscopic properties of brain tissue such as cell density, fiber radius and directionality, myelin, and iron concentration (Fukunaga et al., 2010; Lutti et al., 2014; Weiskopf et al., 2015; Jelescu et al., 2020). Biophysical models of the relationship between tissue microstructure and the MRI signal allow the assessment of microscopic properties of brain tissue from *in vivo* MRI data (“*in vivo* histology”) (Weiskopf et al., 2015; Edwards et al., 2018; Kiselev and Novikov, 2018; Jelescu et al., 2020). Since MRI gives rise to a variety of image contrasts, each contrast being differentially sensitive to multiple microscopic properties of brain tissue, such biophysical models are intrinsically tuned to specific types of MR images (MacKay and Laule, 2016; Does, 2018; Kiselev and Novikov, 2018; Jelescu et al., 2020). Here, we focus on axonal radius and myelination and on the main biophysical models that allow their measurement from *in vivo* data.

Axonal radius is a key property of neurons and is the main determinant of the speed of conduction of action potentials along axonal fibers (Rushton, 1951; Waxman and Bennett, 1972). Axonal radius plays an essential role in neuronal communications and is an instrumental structural underpinning of brain function (Liewald et al., 2014). Axonal radius estimates have been used as measures of functional connectivity in generative models of brain function, e.g., using dynamic causal modeling (Stephan et al., 2009; Honey et al., 2010). Moreover, axonal radius is a biomarker of brain development and healthy aging (Weiskopf et al., 2015) and is of high clinical relevance for a range of disorders such as autism (Wegiel et al., 2018), multiple sclerosis (Evangelou et al., 2001) and motor-neuron disease (Cluskey and Ramsden, 2001). Diffusion contrast is the main type of MRI data used for the measurement of axonal radius *in vivo*. Suitable biophysical models include AxCaliber (Assaf et al., 2008; Barazany et al., 2009), which enables the estimation of the full distribution of axonal radius. ActiveAx is an alternative model that enables the estimation of axonal radius in all white matter tracts without *a priori* knowledge of fiber orientation (Alexander et al., 2010). However, this model provides a single summary index of axonal radius distribution, weighted toward larger axons (Jones et al., 2018; Veraart et al., 2020). Axonal radius estimates obtained *in vivo* from diffusion MRI data are often overestimated compared to histological values (Aboitiz et al., 1992; Liewald

et al., 2014) due to the limited gradient strength of MRI scanners and other confounding factors, such as the dominance of the extra-axonal signal (Burcaw et al., 2015; Nilsson et al., 2017; Jones et al., 2018; Lee et al., 2018; Jelescu et al., 2020; Veraart et al., 2020).

Besides axonal radius, axonal fiber myelination is also a crucial factor in the transmission of neuronal information and brain function (MacKay and Laule, 2016). The non-invasive assessment of myelination enables the study of brain plasticity in healthy individuals and brain changes in a range of neurological disorders (Lazari and Lipp, 2021). Relaxometry MRI data are *in vivo* biomarkers of bulk myelin concentration within brain tissue (Lutti et al., 2014; Stüber et al., 2014). While their validity is supported by a large array of empirical evidence, these biomarkers lack an explicit link with the underlying histological properties of brain tissue, consequently hindering the interpretability of results (Weiskopf et al., 2015). Further specificity may be gained from MRI measures of the fraction of water embedded within the myelin sheath (Feintuch et al., 2007; MacKay and Laule, 2016; Does, 2018). Nonetheless, important aspects pertaining to exchange between compartments and suitable MRI acquisition sequences remain unclear (Dortch et al., 2013). Another effort toward improved specificity lies in MRI measures of the g-ratio, the relative thickness of the myelin sheath around axons (Stikov et al., 2011, 2015). MRI-measured g-ratio estimates are aggregate measures of the axonal g-ratio, across all fibers present in each voxel of an MR image (West et al., 2016).

In summary, current MRI markers of axonal radius and fiber myelination are averages across populations of axons present in each voxel of an MR image. To date, estimating the distribution of these morphological features across axonal populations remain largely out of reach. To address this limitation, we propose a novel approach that enables the estimation, from *in vivo* data, of the radius and myelination of axonal fibers, across the distribution of axonal populations in a white matter tract. This approach is based on the combination of electroencephalography (EEG) measures of signal conduction velocity along a white matter tract of interest, and of MRI measures of the g-ratio, sampled along the same tract. MRI and EEG have been jointly used in brain connectivity studies and for the combined study of brain structure and function (Westerhausen et al., 2006; Sui et al., 2014; Helbling et al., 2015; Horowitz et al., 2015; Deslauriers-Gauthier et al., 2019). In particular, the high temporal resolution of EEG allows the estimation of the interhemispheric transfer time (IHTT) (Saron and Davidson, 1989; Marzi, 1999) using the established visual Poffenberger paradigm (Westerhausen et al., 2006; Whitford et al., 2011; Friedrich et al., 2017; Chaumillon et al., 2018). Subsequently, an estimate of axonal conduction

velocity can be computed (Caminiti et al., 2013; Horowitz et al., 2015). The dominant contributions of axonal radius and myelination to conduction velocity (Drakesmith et al., 2019) underline the complementarity of this EEG measure with the MRI measures described above. In the first part of this paper, we present the biophysical model underlying the proposed approach (Figure 1). Numerical simulations are then conducted to illustrate the plausibility of our results in light of the histology literature and to assess the variability and accuracy of the morphological estimates. To illustrate the feasibility of the proposed approach, we present estimates of axonal morphology obtained using *in vivo* data from the visual transcallosal white matter tract of healthy volunteers.

THEORY—BIOPHYSICAL MODEL

Axon Morphological Properties

With the proposed model (Figure 1), both the MRI and EEG data are described as a function of the distribution of axonal radius $P(r)$ and of the axonal g-ratio $g(r)$ within a given white matter tract. The axonal radius distribution is assumed to be a Gamma distribution (Sepehrband et al., 2016):

$$P(r) = P(r|M, \theta) = \frac{1}{\Gamma(\frac{M}{\theta}+1)\theta^{\frac{M}{\theta}+1}} r^{\frac{M}{\theta}} e^{-\frac{r}{\theta}} \quad (1)$$

where r is the axonal radius. M represents the mode, i.e., the peak of the axonal radius distribution and the parameter θ represents the width of the right tail of the axonal radius distribution, a measure of the number of large axons in a white matter fiber tract.

Histological studies have shown that larger axons exhibit comparatively thinner myelin sheaths, i.e., larger g-ratios (Ikeda and Oka, 2012; Gibson et al., 2014). From data obtained in the peripheral nervous system of the rat, the radius dependence of the g-ratio was shown to follow (Ikeda and Oka, 2012): $g_{REF}(r) = 0.22 \log(2r) + 0.508$. However, to facilitate the mathematical manipulation of the biophysical model (Eqs. 3 and 5 below), we write the radius dependence of the axonal g-ratio as:

$$g(r) = \beta * r^\alpha \quad (2)$$

With this power law, the exponent α represents the slope of the radius dependence of the axonal g-ratio, while the parameter β is a scaling factor. Unlike the mathematical expression for g_{REF} , this power law does not include an offset term. To verify its validity, we fitted this power law with the reference relationship (g_{REF}) of Ikeda and Oka (2012). The result shows an excellent level of agreement between both expressions ($R^2 = 0.99$), with $\alpha = 0.18$ and $\beta = 0.57$ (Figure 2A). We also verified the applicability of the power law in the human central nervous system, where the higher axonal g-ratio requires the addition of a systematic offset to g_{REF} . We estimated this offset to be 0.14, assuming a g-ratio of 0.7 for an axonal radius of 0.9 μm , based on studies showing g-ratio estimates between 0.65 and 0.79 (Mohammadi et al., 2015; Stikov et al., 2015) across the range of axonal radius observed in the human brain (Aboitiz et al., 1992; Caminiti et al., 2009; Liewald et al., 2014). Fitting of the power law (Eq. 2) with the

reference relationship (g_{REF}) after addition of this offset leads to an excellent agreement ($R^2 = 0.99$), with $\alpha = 0.14$ and $\beta = 0.71$ (Figure 2B). The latter values will be used when the parameters α and β are set constant to allow for the estimation of other model parameters (see section “Model Parameters”).

Modeling of the *in vivo* Data

In agreement with West et al. (2016), the MRI-measured g-ratio is written as an ensemble average of the axonal g-ratios within each image voxel, weighted by the axons' cross-sectional area:

$$g_{MRI}^2 = \frac{\int_0^\infty R^2 g(r)^2 P(r) dr}{\int_0^\infty R^2 P(r) dr} = \frac{\int_0^\infty r^2 P(r) dr}{\int_0^\infty \frac{r^2}{g(r)^2} P(r) dr} \quad (3)$$

where R is the fiber radius [$R = r/g(r)$]. From Eqs. (1) and (2), Eq. (3) becomes (see Supplementary Appendix A):

$$g_{MRI}^2 = \beta^2 \theta^{2\alpha} * \frac{\Gamma(\frac{M}{\theta}+1)}{\Gamma(\frac{M}{\theta}+1-2\alpha)} * \frac{M+3\theta+2\frac{\theta^2}{M}}{M+(3-4\alpha)\theta+(2+4\alpha^2-6\alpha)\frac{\theta^2}{M}} \quad (4)$$

As described in Waxman and Bennett (1972), axonal conduction velocity (v) can be derived from the morphological properties of axons using: $v [m/s] = p \frac{d [\mu m]}{g}$, where p (~ 5.5 – 6.0) represents the contribution of additional axonal factors to the propagation of action potentials (e.g., length of Ranvier nodes, electrical properties of the myelin membranes). Assuming an equal contribution from all axons to the conduction velocity V measured with EEG, we obtain:

$$V = 5.5 \int_0^\infty \frac{2r P(r)}{g(r)} dr \quad (5)$$

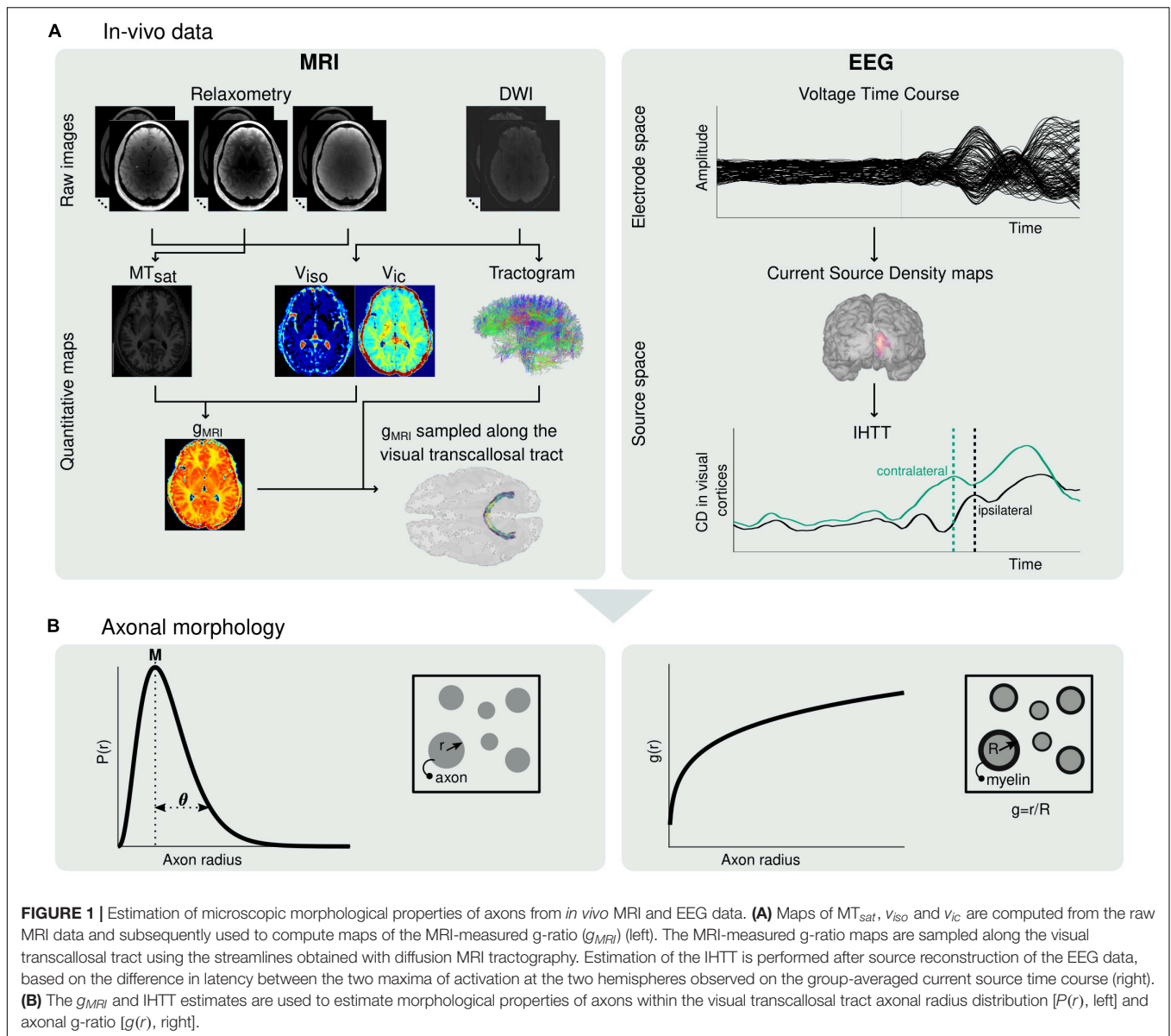
From Eqs. (1) and (2), Eq. (5) becomes (see Supplementary Appendix A):

$$V = \frac{11\theta^{1-\alpha}}{\beta} \frac{\Gamma(\frac{M}{\theta}+1-\alpha)}{\Gamma(\frac{M}{\theta}+1)} \left(\frac{M}{\theta} + 1 - \alpha \right) \quad (6)$$

Model Parameters

The proposed model (Eqs. 4 and 6) includes 4 free parameters, pertaining to the distribution of axonal radius (M and θ) and to the radius-dependent axonal g-ratio (α and β). However, our proposed model uses only two data types acquired *in vivo* (MRI-measured g-ratio and EEG-based axonal conduction velocity). It is therefore necessary to set two parameters to reference values.

In general terms, the choice of model parameters to estimate should take into consideration the neural mechanisms underlying each application study of this model. The exponent α of the power law $g(r)$ represents the rate of change in thickness of the myelin sheath with axonal radius and may be a parameter of interest when considering changes in neuronal shape that differentially affect axons of different sizes. In contrast, the scale parameter β equally affects axons of all sizes. Concerning the distribution of axonal radius, we highlight that histological studies across white matter tracts and animal species have reported that, for reasons pertaining to brain size limitations and metabolism, the mode M of the axonal radius distribution remains largely constant (Tomasi et al., 2012; Liewald et al., 2014). This motivates setting M to a constant value from the



histological literature and estimating the tail parameter θ from the *in vivo* data.

The choice of constant model parameters may also be guided by the impact of inaccurate constant values on the estimated morphological features. The bias of the parameter estimates arising from inaccuracies of 10% in α , M or β was evaluated using numerical simulations (with the procedure described in methods section “Estimation of Axonal Morphology From *in vivo* Data”). Across a range of plausible g_{MRI} and V , an inaccuracy of 10% in α leads to an average bias of ~ 10 and $\sim 15\%$ on the estimated M and θ , respectively (**Supplementary Figure 1A**). Similarly, an inaccuracy of 10% in M leads to an average bias of ~ 1 and $\sim 22\%$ for β and θ , respectively (**Supplementary Figure 1B**). However, an inaccuracy of 10% in β leads to an average bias of $\sim 155\%$ and $\sim 92\%$ for M and θ , respectively (**Supplementary Figure 1C**).

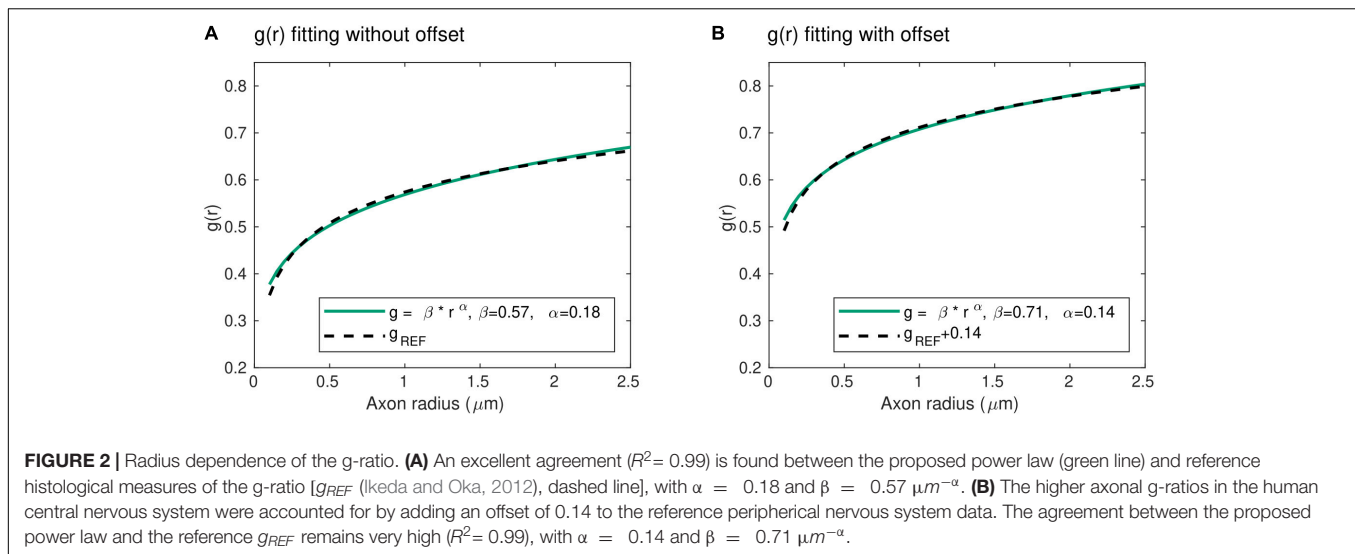
From the biological and numerical considerations above, in this study, we chose to set α to 0.14 (see section “Axon Morphological Properties”) and M to $0.40 \mu\text{m}$ (Tomasi et al., 2012; Liewald et al., 2014) and to estimate the parameters β and θ .

MATERIALS AND METHODS

Numerical Simulations

Numerical simulations were conducted using Eqs. (4) and (6), to examine the values of the model parameters (M , θ , α , and β) obtained from combinations of the *in vivo* data (g_{MRI} and V) using the procedure described in methods section “Estimation of Axon Morphology From *in vivo* Data”, and vice versa.

In order to highlight the range of *in vivo* data values compatible with the proposed model, estimates of M and θ were



computed across a large range of g_{MRI} and V values, setting $\alpha = 0.14$ and $\beta = 0.71$ (section “Axon Morphological Properties”). The range of *in vivo* data values compatible with the proposed model was determined by comparison of the M and θ estimates against reference literature values.

Subsequent numerical simulations were conducted by estimating the parameters β and θ across the range of compatible *in vivo* data values, setting $\alpha = 0.14$ and M to $0.40 \mu m$ (section “Model Parameters”). In particular, we examined the range of the parameters β and θ across values of g_{MRI} and V reported in the literature.

The variability of the model parameter estimates in the presence of noise was also investigated. Simulated estimates of the *in vivo* data g_{MRI} and V were computed from combinations of θ and β values using Eqs. (4) and (6). Noise was added to the computed g_{MRI} and V values with a standard deviation of 0.03 for g_{MRI} and 0.50 m/s for V , representative of intra-subject variability in *in vivo* data. To replicate *in vivo* conditions, 700 samples of g_{MRI} and one sample of V were taken from the resulting distributions of g_{MRI} and V , and estimates of θ and β from noisy data were calculated. This process was repeated 2,000 times and the standard deviation of the θ and β estimates across repetitions was computed as a measure of their variability.

Finally, we set out to investigate the effect of using a group averaged conduction velocity rather than subject-specific velocities. We selected 15 samples of g_{MRI} and V values from distributions with means of 0.70 and 10 m/s and standard deviations of 0.05 and 0.80 m/s, respectively, representative of inter-subject variability in *in vivo* data. From these simulated *in vivo* data, reference values of β and θ were calculated. Estimates of β and θ were also computed from the average of the 15 samples of V . We then estimated the bias between the reference β and θ values and those obtained from the average value of V .

In vivo Data

We acquired data from 17 right-handed healthy volunteers. All participants had normal or corrected-to-normal vision

and hearing and had no history of psychiatric or neurological disorders. Participant handedness was evaluated with the Edinburgh Handedness Inventory (Oldfield, 1971). All participants gave written informed consent and received 80 Swiss Francs as monetary compensation. The study was approved by the local ethics committee.

MRI data quality was assessed using the Motion Degradation Index (MDI) described in Castella et al. (2018) and Lutti et al. (2022). MDI values were $\lesssim 4 s^{-1}$ for the PD- and T1-weighted raw images, and $\lesssim 5 s^{-1}$ MT-weighted raw images, indicative of good quality images (Lutti et al., 2022; see **Supplementary Figure 2**). Three participants were excluded due to artifacted EEG recordings. The final sample consisted of 14 participants (6 females; age = 27.14 ± 3.86 years). Three participants had left eye dominance, as determined by the eye viewing an object at a distance when the participant looks through a small opening (Miles, 1930). An overview of the data processing pipeline of the *in vivo* data is shown in **Figure 1A**.

Magnetic Resonance Imaging-Based Estimation of the G-Ratio

MRI data were collected on a whole-body 3T MRI system (Magnetom Prisma; Siemens Medical Systems, Erlangen, Germany) using a 64-channel receive head coil at the Laboratory for Neuroimaging Research, Lausanne University Hospital.

Structural Magnetic Resonance Imaging Acquisition

A 3D structural T1-weighted Magnetization-Prepared Rapid Gradient-Echo (MPRAGE) image was acquired with a $1 mm^3$ isotropic voxel size and a matrix size of $176 \times 232 \times 256$. TR/TE = 2,000/2.39 ms. TI/ α = 920 ms/ 9° . Parallel imaging (acceleration factor 2, GRAPPA reconstruction) was used along the phase-encoding direction (Griswold et al., 2002). The total acquisition time was 4 min.

Relaxometry Magnetic Resonance Imaging Acquisition

The relaxometry MRI protocol consisted of multi-echo 3D fast low angle shot (FLASH) acquisitions with magnetization

transfer-weighted ($TR/\alpha = 24.5 \text{ ms}/6^\circ$, 6 echos), proton density-weighted ($TR/\alpha = 24.5 \text{ ms}/6^\circ$, 8 echos) and T1-weighted ($TR/\alpha = 24.5 \text{ ms}/21^\circ$, 8 echos) (Melie-Garcia et al., 2018) image contrasts (Figure 1A). The echo spacing and minimal echo time were both 2.34 ms. The MR images had a 1 mm^3 isotropic voxel size. Parallel imaging (acceleration factor 2, GRAPPA reconstruction) was used along the phase-encoding direction (Griswold et al., 2002) and Partial Fourier (acceleration factor 6/8) was used along the partition direction. B1-field mapping data was acquired to correct for RF transmit field inhomogeneities (Lutti et al., 2010, 2012): 4 mm^3 voxel size, $TR/TE = 500/39.1 \text{ ms}$. B0-field mapping data was acquired to correct for image distortions in the B1 mapping data: 2D double-echo FLASH, $TR/\alpha = 1,020 \text{ ms}/90^\circ$, $TE1/TE2 = 10/12.46 \text{ ms}$, $BW = 260 \text{ Hz/pixel}$, slice thickness = 2 mm. The total acquisition time was 27 min.

Diffusion-Weighted Imaging

Diffusion-weighted imaging (DWI) data were acquired using a 2D echo-planar imaging sequence ($TR/TE = 7,420/69 \text{ ms}$) along 15, 30, and 60 diffusion directions with $b = 650/1,000/2,000 \text{ s/mm}^2$, respectively (Figure 1A). 13 images with $b = 0$ were acquired, interleaved throughout the acquisition (Slater et al., 2019), making a total of 118 isotropically distributed directions. Images had a 2 mm^2 isotropic voxel size and a matrix size of 96×106 , with 70 axial slices. Parallel imaging was used along the phase-encoding direction (acceleration factor 2, GRAPPA reconstruction). The total acquisition time was 15 min.

Estimation of Magnetic Resonance Imaging Quantitative Maps

Maps of Magnetization Transfer (MT_{sat}) were computed from the raw FLASH images as in Helms et al. (2008a,b) (Figure 1A). The map computation was conducted using the hMRI toolbox (Tabelow et al., 2019) and included corrections for local RF transmit field inhomogeneities (Helms et al., 2008a) and for imperfect RF spoiling (Preibisch and Deichmann, 2009).

DWI data were corrected for geometrical distortions, using *eddy* from FMRIB's Diffusion Toolbox (Andersson and Sotiropoulos, 2016), and for echo-planar imaging susceptibility distortions using the SPM12 fieldmap toolbox (Hutton et al., 2002). DWI images were aligned to the MT_{sat} map using SPM12 and a rigid body transformation. Finally, maps of the isotropic diffusion (v_{iso}) and intracellular (v_{ic}) compartments volume fractions were computed from the DWI data using the NODDI model (Zhang et al., 2012) and the AMICO toolbox (Daducci et al., 2015; Figure 1A).

Maps of the MRI-measured g-ratio were estimated from: $g_{MRI} = \sqrt{1/(1 + MVF/AVF)}$, where MVF and AVF are the myelin and the axonal volume fractions, respectively (Stikov et al., 2015; Figure 1A). The MVF maps were estimated from the MT_{sat} maps according to: $MVF = \alpha MT_{sat}$, where the calibration factor α was set by assuming a median g_{MRI} value of 0.70 in the splenium of the CC of 11 subjects of a separate cohort ($\alpha = 0.23$) (Campbell et al., 2018; Slater et al., 2019). The AVF maps were estimated as: $AVF = (1 - \alpha MT_{sat}) / (1 - v_{iso})v_{ic}$ (Stikov et al., 2015).

The Freesurfer 6.0 software (Schiffler et al., 2017) was used to delineate each subject's Brodmann areas 17 and 18 (Fischl et al., 2008) from their MPRAGE image, corresponding to the primary (V1) and secondary (V2) visual cortical areas, respectively. These regions of interest (ROIs), henceforth called "V1V2", were grouped and registered to the diffusion data using FMRIB's Linear Image Registration Tool (Jenkinson and Smith, 2001).

Tractography analysis was conducted using the mrTrix software (Tournier et al., 2019): whole-brain anatomically constrained tractography was performed using the iFOD2 algorithm, with dynamic seeding to improve the distribution of reconstructed streamlines density, a maximum of 45° between successive steps, a cut-off of 0.05 in the fiber orientation distribution amplitude, backtrack and streamlines cropping in the gray-white matter interface. A total of 20 million streamlines between 5 and 250 mm in length were selected and submitted to SIFT2 to penalize streamlines with a reduced agreement with diffusion data. The visual transcallosal tract was isolated by selecting the streamlines connecting the V1V2 ROIs in each hemisphere across the CC. This tract was used to extract samples from the MRI-measured g-ratio maps (Figure 1A).

Electroencephalography-Based Estimation of the Interhemispheric Transfer Time

Experimental Paradigm

We implemented the visual Poffenberger paradigm on a 61 cm widescreen (60 Hz refreshing rate), in line with the literature (Westerhausen et al., 2006; Whitford et al., 2011; Friedrich et al., 2017; Chaumillon et al., 2018). The experiment was administered using Psychtoolbox-3.0.16 in MATLAB (R2019b, The Mathworks, Natick, MA). Participants were comfortably seated on a chair in a dimly lit room, at a standardized distance of 80 cm from the screen, thus 1 cm on the screen represented 0.72° of the visual angle. Each trial consisted of the presentation of a black and white circular checkerboard with a pattern reversal of 15 Hz on a gray background (20 cd/m^2) and with a duration of 100 ms. The stimuli were of 4° diameter and their outer edge appeared at 6° horizontal and 6° vertical distance from the centrally-located fixation cross (0.8° size) to the lower left or right visual hemifield. The acquisition was structured in 6 blocks with an approximate duration of 6 min each; a short break was allowed between each experimental block. Each block consisted of 205 trials (95 for right visual field, 95 for left visual field, and 15 where no stimulus appeared), presented in a pseudorandom order and with inter-trial intervals randomly assigned between 1.0 and 2.0 s. Participants were instructed to avoid unnecessary movements and to press a button as quickly as possible after the appearance of a stimulus while keeping their gaze on the fixation cross. Responses were given with the index finger via a keyboard button press placed centrally to the subject's body. The administered blocks alternated between left and right-hand index finger button presses (three blocks per hand).

Electroencephalography Data Acquisition

Continuous 128-channel EEG was recorded using the Micromed recording system (Micromed SystemPlus Evolution, Mogliano

Veneto, Italy) and an Ag/AgCl electrode cap (waveguard™ original, ANT Neuro, Hengelo, Netherlands) at a sampling rate of 1,024 Hz with FPz as the reference electrode and AFFz as the ground electrode. Two additional horizontal EOG electrodes were attached to the outer canthi of each eye. Electrode impedance was kept below 20 k Ω . Electrode positions and head shape were acquired for each participant using the xensor™ digitizer (ANT Neuro, Hengelo, Netherlands).

Electroencephalography Data Analysis

EEG data analysis utilized custom-made MATLAB (R2021a, The Mathworks, Natick, MA) scripts and open-source toolboxes Fieldtrip (version 20191206, Oostenveld et al., 2011), EEGLAB (version 13.4.4b, Delorme and Makeig, 2004), and Brainstorm (Tadel et al., 2011). Continuous raw EEG was bandpass-filtered between 0.1 and 40 Hz (digital filters). EEG epochs were extracted from the filtered data ranging from -100 to 300 ms relative to visual stimulus onset. Artifact trials were removed based first, on visual inspection. Next, we identified and removed components containing eye movement related artifacts by running an Independent Component Analysis based on the *runica* algorithm (Bell and Sejnowski, 1995). Epochs containing additional artifacts were identified based on a threshold of 80 μ V and excluded from further analysis. Across participants, an average of 20.5% (SD: 10.1%, range: 43–220 trials) and 21.3% (SD: 11.0%, range: 42–206 trials) of the trials were rejected for the left and right visual field stimulation, respectively. Artifact electrodes were identified based on a threshold of 80 μ V and were interpolated using the nearest neighbors. On average, 5.9% of electrodes (SD: 2.4%, range 3–14 electrodes) were interpolated across participants. EPOCHED data were re-referenced to the average reference. We removed DC drift by subtracting the average within each epoch.

Source reconstruction was performed to identify the neural origins underlying the visual evoked response to the left and right hemifield visual stimuli (Figure 1A). Virtual sensors from artifact-free EEG data were calculated using the minimum-norm current density method (Hämäläinen and Ilmoniemi, 1994) as implemented in Brainstorm. The MRI image of each subject was registered to the electrode positions using an iterative algorithm that finds the best fit between the head shape obtained using the MRI data and that obtained via EEG digitization. Surface reconstructions were obtained using a 3-layer Boundary Element Method (Kybic et al., 2005; Gramfort et al., 2010) model on each subject's MRI image. The source grid was defined with 15,000 points on the gray matter. This way, we estimated the current densities (CD, pA.m) for each condition, source, and time point within each subject. The CDs were extracted for the V1V2 ROI defined in section "MRI-Based Estimation of the G-Ratio" — for the left and right brain hemisphere — for each trial and each subject. Next, V1V2 ROI CDs were averaged across trials within each subject. Given that cortical anatomies vary considerably across participants due to the folding patterns of each individual, current source density maps have ambiguous signs on the group level. Consequently, we took the absolute value of the CDs of each subject before computing a group average.

Estimation of the Interhemispheric Transfer Time and Conduction Velocity

We assumed that lateralized visual stimuli would induce first, a contralateral activation of the visual cortex, followed by an activation of the ipsilateral cortex. This visual information transfer is assumed to be achieved through the CC (Marzi, 1999).

For the IHTT estimation, we identified the first peaks of activation in each hemisphere based on the maximum of the average current density value at the group level (Figure 1A). IHTT was calculated as the latency difference between the ipsilateral and contralateral activation peaks on the group average CDs within the V1V2 ROI. A Wilcoxon signed-rank test ($p < 0.05$; *signrank*, in MATLAB) comparing the CDs across participants at these two maxima to the time-average baseline values was used to evaluate the significance of these activations as evoked activity in response to the visual stimuli.

To obtain a confidence interval on the computed IHTT, we subdivided the artifact-free EEG trials available for each participant into four non-overlapping splits. We then repeated four times the CD estimation at group-level where each subject contributed with data coming from one of the split in order to obtain four independent estimations of the IHTT. This allowed us to obtain a standard deviation on the IHTT estimation, which we used to define a confidence interval on the IHTT estimation: [*IHTT-standard deviation*; *IHTT+standard deviation*].

Of note, we assumed that the right eye dominance of the majority of the included participants elicited a more reliable estimation of the evoked activity following the left visual stimuli in comparison to the right. For this reason, here, we used the IHTT estimation following the left hemifield visual stimuli.

At the individual level, we extracted the visual transcallosal tract length as the tractography-based mean streamline length. V was calculated by dividing the tract length by the IHTT.

Estimation of Axonal Morphology From in vivo Data

Estimation of axonal morphological features from the *in vivo* MRI and EEG data was implemented using MATLAB-based custom-made analysis scripts. The MRI-measured g-ratio samples along the visual transcallosal tract and the estimate of the IHTT were used to estimate model parameter values using Eqs. (4) and (6) (see section "Axon Morphological Properties", Figure 1B). This was achieved using MATLAB's non-linear least-square routine (*lsqnonl*) with a trust-region-reflective minimization, which minimizes the sum of the squares of the residuals. The initial conditions used to ensure convergence of the fitting routine were set to $\beta = 0.70 \mu\text{m}^{-\alpha}$ and $\theta = 0.10 \mu\text{m}$.

All codes are available on our online repository: <https://github.com/LREN-physics/AxonalMorphology>.

RESULTS

Numerical Simulations

We investigated the range of *in vivo* data compatible with the proposed model by considering the values of the model

parameters M and θ computed from each combination of g_{MRI} and V (Figure 3). Combinations of large values of g_{MRI} and low values of V lead to unrealistically low values of M ($\sim 10^{-14}$ μm). Conversely, small values of g_{MRI} and large values of V lead to excessively large values of M (~ 1 μm) and low values of θ (~ 0.001 μm) (Aboitiz et al., 1992; Caminiti et al., 2009, 2013; Tomasi et al., 2012; Liewald et al., 2014).

Figure 4 shows the range of the model parameters θ and β across a large range of g_{MRI} and V values. According to the literature, frontal transcallosal white matter exhibits MRI-measured g-ratio values of ~ 0.62 (Mohammadi et al., 2015; Slater et al., 2019) and conduction velocities of ~ 8 m/s (Caminiti et al., 2013; see red cross in Figure 4A). The proposed model yields $\theta \sim 0.05$ μm for such combination of g_{MRI} and V , equivalent to a mean axonal radius of 0.45 μm (Figure 4B). This value is consistent with histological analyses of such white matter fibers, with a narrow range of axonal radius (mean ~ 0.48 μm ; Caminiti et al., 2009). For visual transcallosal white matter (MRI-measured g-ratio ~ 0.72 ; conduction velocity ~ 10 m/s; Caminiti et al., 2013; Mohammadi et al., 2015; Slater et al., 2019), the proposed model yields $\theta \sim 0.23$ μm (see black cross in Figure 4A), leading to a mean axonal radius of ~ 0.63 μm (Figure 4B). This value is also consistent with histological analyses of such white matter fibers, with a broad range of axonal radius (mean ~ 0.62 μm ; Caminiti et al., 2009). For both types of white matter tracts, fibers with a radius above 1.5 μm represent less than 4% of the total number of fibers, consistently with previous histological studies (Aboitiz et al., 1992; Caminiti et al., 2009; Liewald et al., 2014). The value of the model parameter β for frontal and visual transcallosal white matter were 0.68 and 0.73 $\mu\text{m}^{-\alpha}$, respectively (Figures 4C,D), in line with histological analyses of the axonal g-ratio in the genu and splenium of the CC (Stikov et al., 2015).

Figure 5 shows the variability of the θ and β estimates in the presence of noise in the *in vivo* data, computed from combinations of conduction velocity and MRI-measured g-ratio across a plausible range with 700 g_{MRI} samples and one V sample.

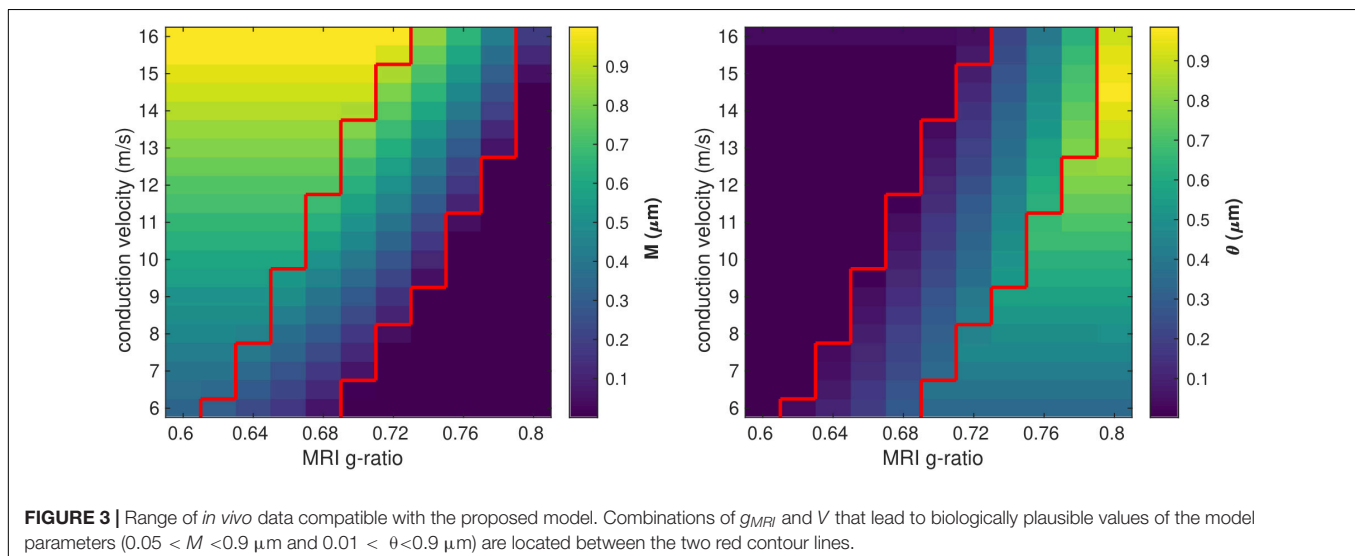
The highest errors in θ ($\sim 35\%$) are found for the smallest values of θ , with only a small effect of the parameter β . The highest errors in β ($\sim 1\%$) are obtained from a combination of small values of θ and large values of β . Supplementary Figure 3 shows the dependence of the variability of the θ and β estimates on the number of samples of V and g_{MRI} ($\beta = 0.71$ $\mu\text{m}^{-\alpha}$ and $\theta = 0.22$ μm). With only one estimate of V , as was the case in this study, errors of up to 11% on the θ estimates are observed. The errors on the β estimates are mostly driven by the number of g_{MRI} samples included in the estimation: for 100 g_{MRI} samples or more, these errors are below 1% regardless of the number of V samples.

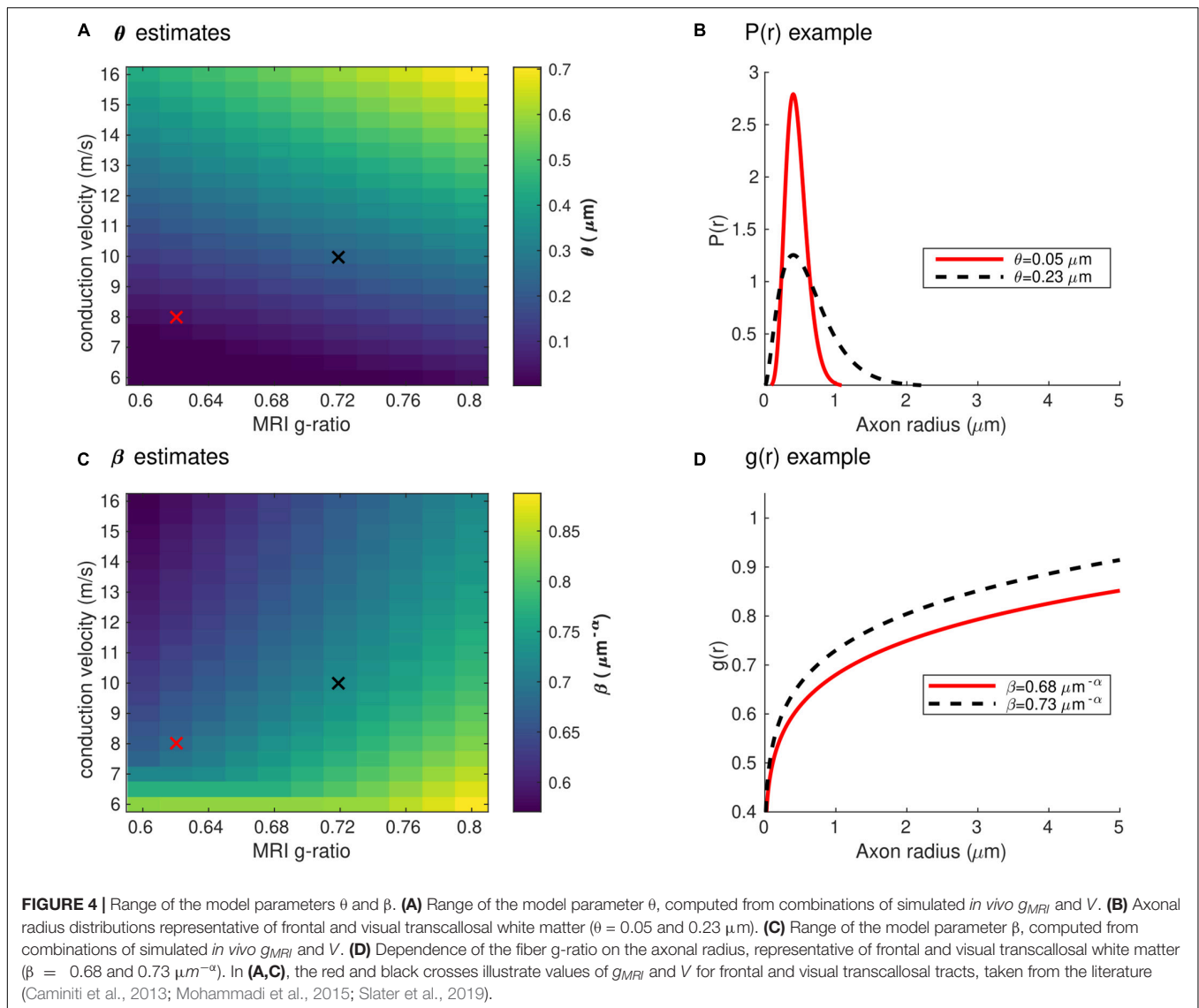
Figure 6 shows the bias in the θ and β estimates arising from an estimation of conduction velocity from a cohort of participants. The bias in θ and β is on average 12 and 0.90% across participants, reaching up to 40 and 3%, respectively.

Estimation of the Interhemispheric Transfer Time and Conduction Velocity

At the sensor level, the group-averaged visual evoked response revealed a positive peak activation, between 115 and 134 ms post-stimulus onset, contralaterally to the stimulus presentation (Figure 7, top). The latency of this positive activation corresponds to the expected latency of the P100 component (Di Russo et al., 2001) and was followed by asymmetrically distributed voltage topographies with maximal voltage values at posterior sites at latencies starting at approximately 153 ms post-stimulus onset (Figure 7, bottom). After approximately 180 ms, post-stimulus onset voltage topographies showed an ipsilateral positivity to the stimulus presentation, suggesting that the P100 activation has traveled to the opposite hemisphere.

Qualitative observations at the electrode-level were confirmed by the source reconstruction results. Group-averaged absolute CD exhibited a sharp increase at approximately 100 ms post-stimulus onset in the right hemisphere compared to the baseline, peaking at 141 ms (Figure 8B for an overview of the spatial





distribution of the CD for an exemplar subject). The group-averaged absolute CD on the left visual hemisphere followed the right visual hemisphere, peaking later on at 152 ms.

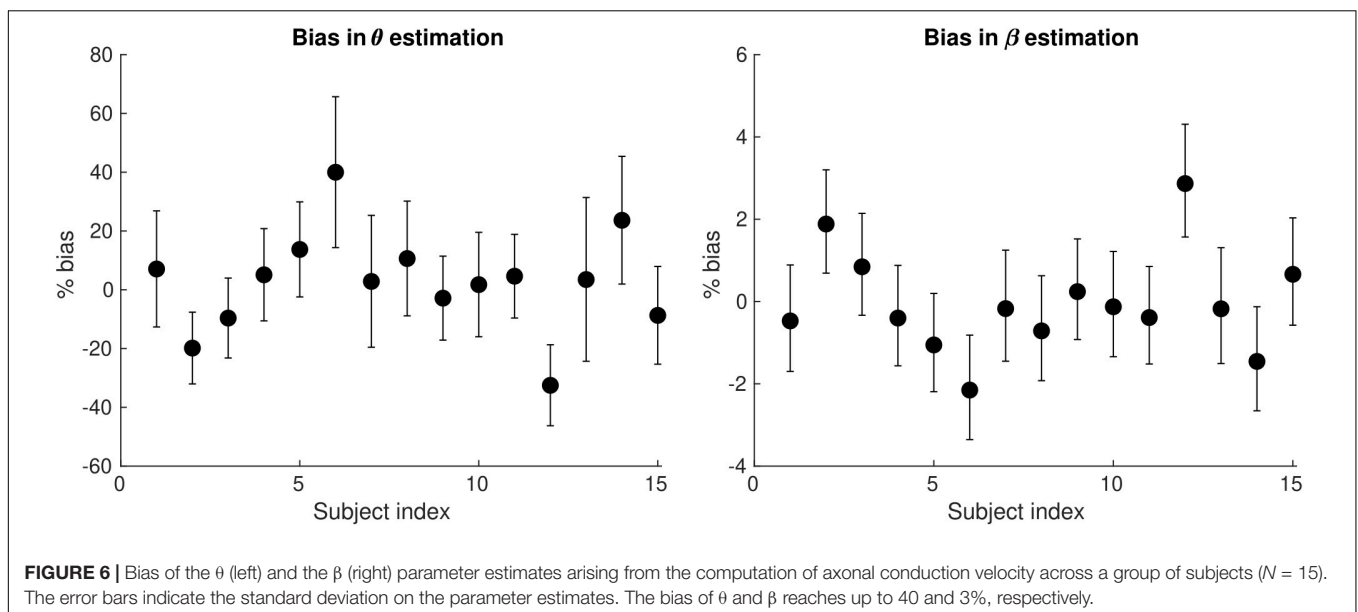
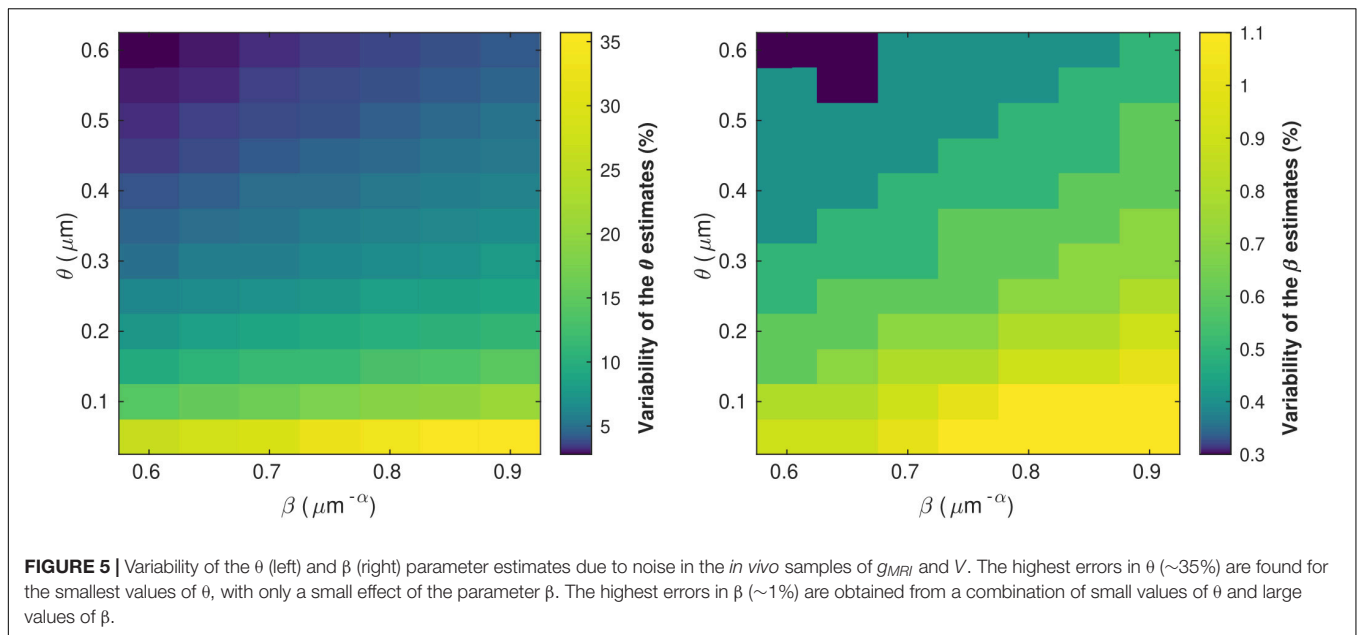
The IHTT group estimation yielded a value of 11.72 ms with a standard deviation of 2.87 ms. The identified peaks were statistically significantly larger upon visual stimulation when compared to the baseline with p -values of $p < 0.01$.

Using the estimated group IHTT, we calculated the conduction velocity for the visual transcallosal tract using each participant's tract length. The average conduction velocity was 13.22 ± 1.18 m/s across participants (Table 1).

Estimation of Axonal Morphology From *in vivo* Data

Estimates of the model parameters θ and β were computed using the proposed model, from the *in vivo* samples of the MRI-measured g -ratio along the visual transcallosal tract and

estimates of conduction velocity (Table 1). The average value of θ was $0.40 \pm 0.07 \mu\text{m}$ across all subjects and ranged between 0.31 and $0.54 \mu\text{m}$ (Figure 9A). A θ value of $0.40 \mu\text{m}$ is equivalent to a mean axonal radius of $0.80 \mu\text{m}$, in line with previous estimates from histological studies ($0.62 \mu\text{m}$; Caminiti et al., 2009). For such a value of θ , axons with a radius above $2 \mu\text{m}$ represent only $< 5\%$ of the total fiber count, in agreement with histological studies that show that axonal radius does not exceed ~ 1.5 – $3 \mu\text{m}$ in the human brain (Aboitiz et al., 1992; Caminiti et al., 2009; Liewald et al., 2014). The average value of β was $0.67 \pm 0.02 \mu\text{m}^{-\alpha}$ across all subjects, and ranged between 0.64 and $0.70 \mu\text{m}^{-\alpha}$ (Figure 9B). Figure 9C shows the axonal radius distribution $P(r)$ for a representative subject ($\theta = 0.43 \mu\text{m}$), with a confidence interval of 0.27 – $0.69 \mu\text{m}$ obtained from the IHTT estimation. The estimated value of β for this subject was $0.68 \mu\text{m}^{-\alpha}$, with a confidence interval between 0.64 and $0.71 \mu\text{m}^{-\alpha}$ (Figure 9D).

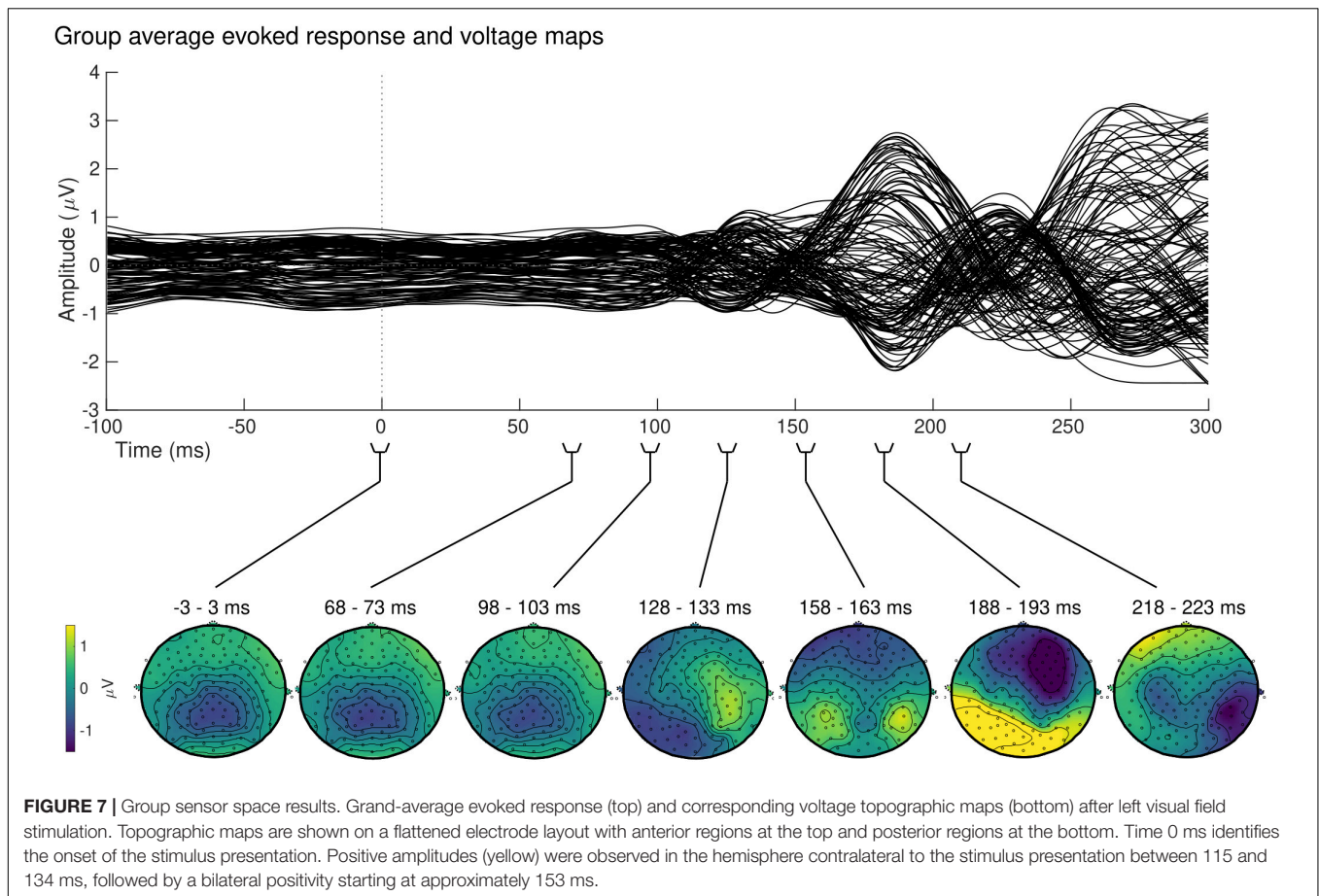


DISCUSSION

In this paper, we propose a novel method that allows the non-invasive estimation of morphological properties of white matter axons from *in vivo* human data. This approach requires MRI-measured g-ratio and EEG-based measures of axonal conduction velocity computed from estimates of the IHTT. From these measures, we estimated the axonal radius and myelination of axonal fibers, distinct histological features of white matter. These morphological features were assessed across the distribution of axons in the visual transcallosal tract, providing a detailed insight into the microscopic properties of these white matter fibers.

Estimation of Axonal Morphology From *in vivo* Data

The proposed model is based on an explicit link between the data acquired *in vivo* and a limited set of histological properties of white matter axons. The MRI-measured g-ratio is expressed as a function of the axonal radius distribution $[P(r)]$ and the g-ratio of axonal fibers $[g(r)]$, inline with recent studies conducted using MRI and histology data (Stikov et al., 2011, 2015; West et al., 2016). Similarly, axonal conduction velocity — computed from the IHTT estimates — is an ensemble average across the same distribution $P(r)$, assuming an equal contribution of all axons to the EEG data. As a result, both types of *in vivo* data depend on the same properties of axonal fibers: $P(r)$ and $g(r)$. This



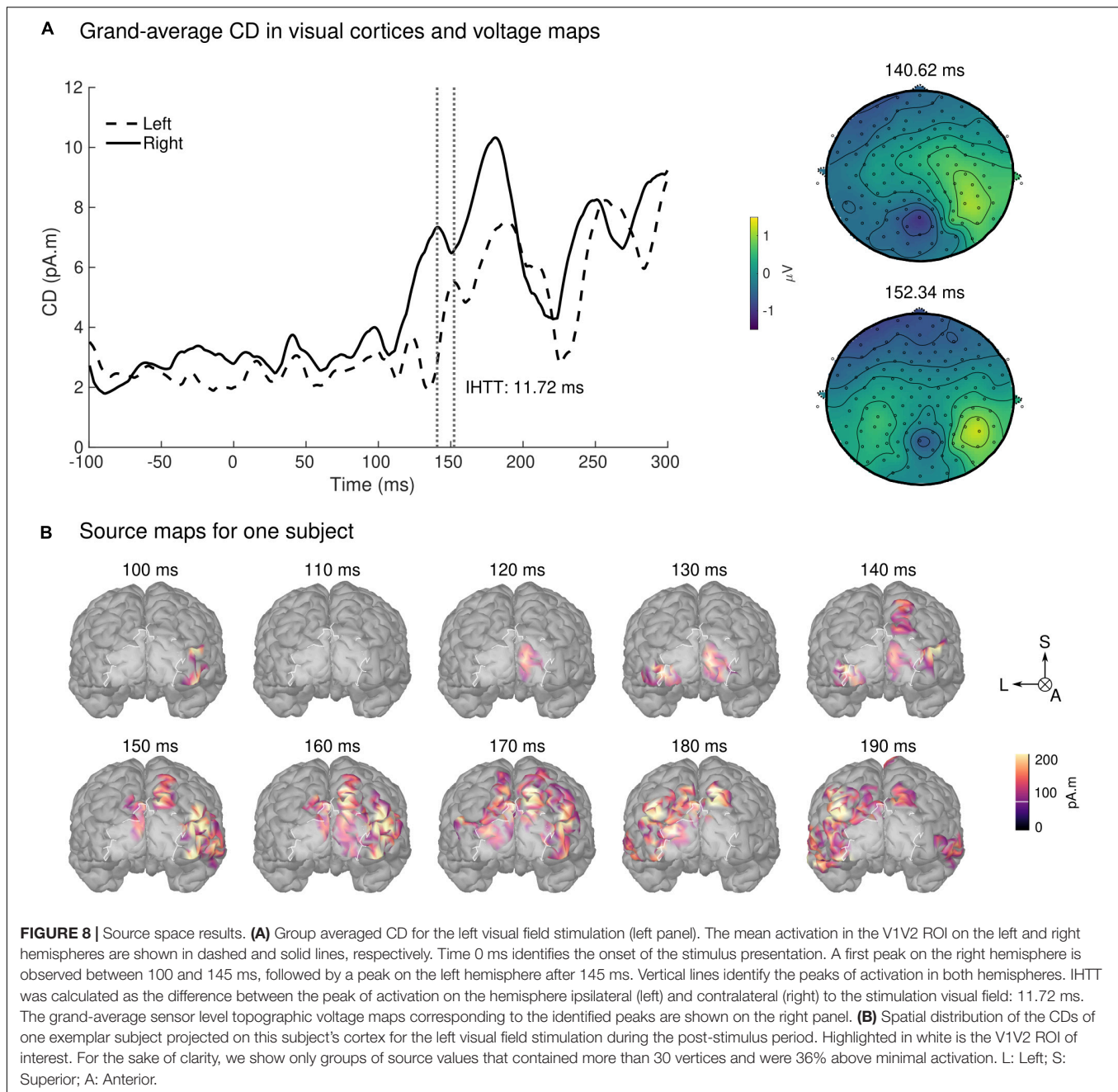
approach is supported by recent findings which show that from the numerous histological determinants of conduction velocity (e.g., axonal radius, g-ratio, the conductance of ion channels, diameter and length of Ranvier nodes and internodes), the properties of axons that bring the largest contribution to the determination of conduction velocity are measurable with MRI (Drakesmith et al., 2019).

The mathematical definitions of $P(r)$ and $g(r)$ are grounded on well-established histological findings. $P(r)$ is assumed to follow a gamma distribution, as commonly posited by models of axonal radius distribution (Assaf et al., 2008; Sepehrband et al., 2016). $g(r)$, expressed using a power law, shows a high level of agreement with histological studies (Ikeda and Oka, 2012; Gibson et al., 2014; **Figure 2**). Besides supporting the proposed model, the histological basis for the expressions of $P(r)$ and $g(r)$ allows freedom in the choice of the model parameters estimated from the data, because they reflect different properties of axon populations that can be set constant or variable according to their relevance in a neuroscience application of this model.

From the set of 4 model parameters, we opted to set the mode M of the axonal radius distribution to a constant value, based on the histological literature (Tomasi et al., 2012; Liewald et al., 2014). Similarly, the parameter α was set from a calibration with histological findings (g_{REF}) (Ikeda and Oka, 2012; see section “Axon Morphological Properties”). The

estimated parameters — θ , the right tail of $P(r)$ and β , the scaling parameter of $g(r)$ — enabled the simultaneous assessment of axonal radius and myelination, across the distribution of axons in the visual transcallosal white matter tract. The average value of θ was $0.40 \mu\text{m}$ across participants, leading to a mean axonal radius of $0.80 \mu\text{m}$, inline with previous estimates from histological studies ($0.62 \mu\text{m}$; Caminiti et al., 2009). The average value of β was $0.67 \mu\text{m}^{-\alpha}$ across participants, consistent with histological measures of the axonal g-ratio in the splenium of the CC (Jung et al., 2018).

The proposed approach inherits the limitations of the MRI methodologies used to estimate the intra-cellular and myelin volume fractions, and subsequently the MRI-measured g-ratio. In the current application, the NODDI model was used to estimate the intra-cellular volume fraction (Zhang et al., 2012). This model assumes identical parallel diffusivity in the extra- and intra-cellular spaces, set to $1.7 \mu\text{m}^2/\text{ms}$ (Zhang et al., 2012). This simplifying assumption might lead to potential bias of the parameter estimates (Jelescu et al., 2015). We estimated that a change in diffusivity within a realistic range ($1.5\text{--}1.9 \mu\text{m}^2/\text{ms}$, Guerrero et al., 2019) leads to a change of 4–5% and 1–2% for θ and β , respectively, smaller than the bias arising from the use of group-averaged conduction velocities (12% for θ and 0.90% for β). Alternatives models (e.g., Assaf and Basser, 2005; Fieremans et al., 2011; Campbell et al., 2018;



Ellerbrock and Mohammadi, 2018) may be considered in light of their assumptions, as well as their applicability given the available data.

Estimation of the Interhemispheric Transfer Time and Conduction Velocity

The IHTT was estimated from the group averaged CDs, which allowed for easy identification of the first two maxima of activation in the two hemispheres (Figure 8). The IHTT derived as a result of the time interval separating the peaks of CDs at the group level (11.72 ± 2.87 ms) falls within the range (i.e., 8 and

30 ms) of previous IHTT estimates based on a *a priori* selection of voltage measurement at electrodes at occipital sites (e.g., Saron and Foxe, 2003; Westerhausen et al., 2006; Whitford et al., 2011; Friedrich et al., 2017; Chaumillon et al., 2018). In our study, we opted for a CD-based estimation of the IHTT as the closest reflection of the evoked neural activity in the regions of interest, consistent with the corresponding white matter tract selection (section "MRI-Based Estimation of the g-ratio"). In addition, this approach helps to overcome the ambiguity of electrode selection in electrode-based IHTT estimations. The resulting estimates of conduction velocity are in agreement with the values reported by Caminiti and colleagues (10 m/s, Caminiti et al., 2013), obtained

TABLE 1 | MRI-measured g-ratios, measured tract length, and estimated conduction velocity with corresponding confidence interval, for each subject in the visual transcallosal tract.

g_{MRI}	Tract length (mm)	Velocity (m/s)	Velocity confidence interval (m/s)
0.69 ± 0.03	155.03	13.23	[10.63; 17.52]
0.71 ± 0.03	149.38	12.75	[10.20; 16.88]
0.71 ± 0.04	133.43	11.38	[9.15; 15.08]
0.69 ± 0.04	136.25	11.63	[9.34; 15.40]
0.67 ± 0.04	154.32	13.17	[10.58; 17.44]
0.69 ± 0.03	171.41	14.63	[11.75; 19.37]
0.71 ± 0.04	157.94	13.48	[10.83; 17.85]
0.71 ± 0.03	149.95	12.79	[10.28; 16.94]
0.69 ± 0.04	152.98	13.05	[10.49; 17.29]
0.68 ± 0.03	142.29	12.14	[9.75; 16.08]
0.68 ± 0.04	155.49	13.27	[10.66; 17.57]
0.69 ± 0.03	172.32	14.70	[11.81; 19.47]
0.69 ± 0.03	184.48	15.74	[12.64; 20.85]
0.69 ± 0.04	154.40	13.17	[10.58; 17.45]

from human histological samples of the same fiber tract. Our results are also consistent with a more recent report that uses a different approach based on Bayesian networks to map the flow of information following left visual stimulation (Deslauriers-Gauthier et al., 2019). The authors observed a transfer of information from the right to the left occipital cortex, between 140 and 160 ms (Deslauriers-Gauthier et al., 2019), in agreement with the latencies of the right and left activations observed in our analysis.

Ideally, IHTT estimates should be performed at the single-subject level to provide microstructure measures specific to each subject. However, the presence of multiple peaks of activation in some individual datasets and the resulting ambiguity in defining the maxima of activation consistently across subjects prevented the estimation of individual IHTT values. These singularities might arise from differences in brain morphology (Saron and Foxe, 2003), inaccurate estimation of the sources, or from the lack of an objective criterion for selecting subjects fulfilling our assumptions on the expected pattern of activations. The difficulty in estimating the IHTT at the subject level has been pointed out in many other studies that showed inconsistent IHTT values across participants and counterintuitively, even negative values in some cases (e.g., Saron and Davidson, 1989; Marzi et al., 1991; Westerhausen et al., 2006; Friedrich et al., 2017). Estimation of the IHTT might be improved with further development on the computation of the inverse solution (Plomp et al., 2010; Mahjoory et al., 2017), and by introducing priors to constrain the time courses of the activations.

Anatomical Substrate for the Interhemispheric Transfer

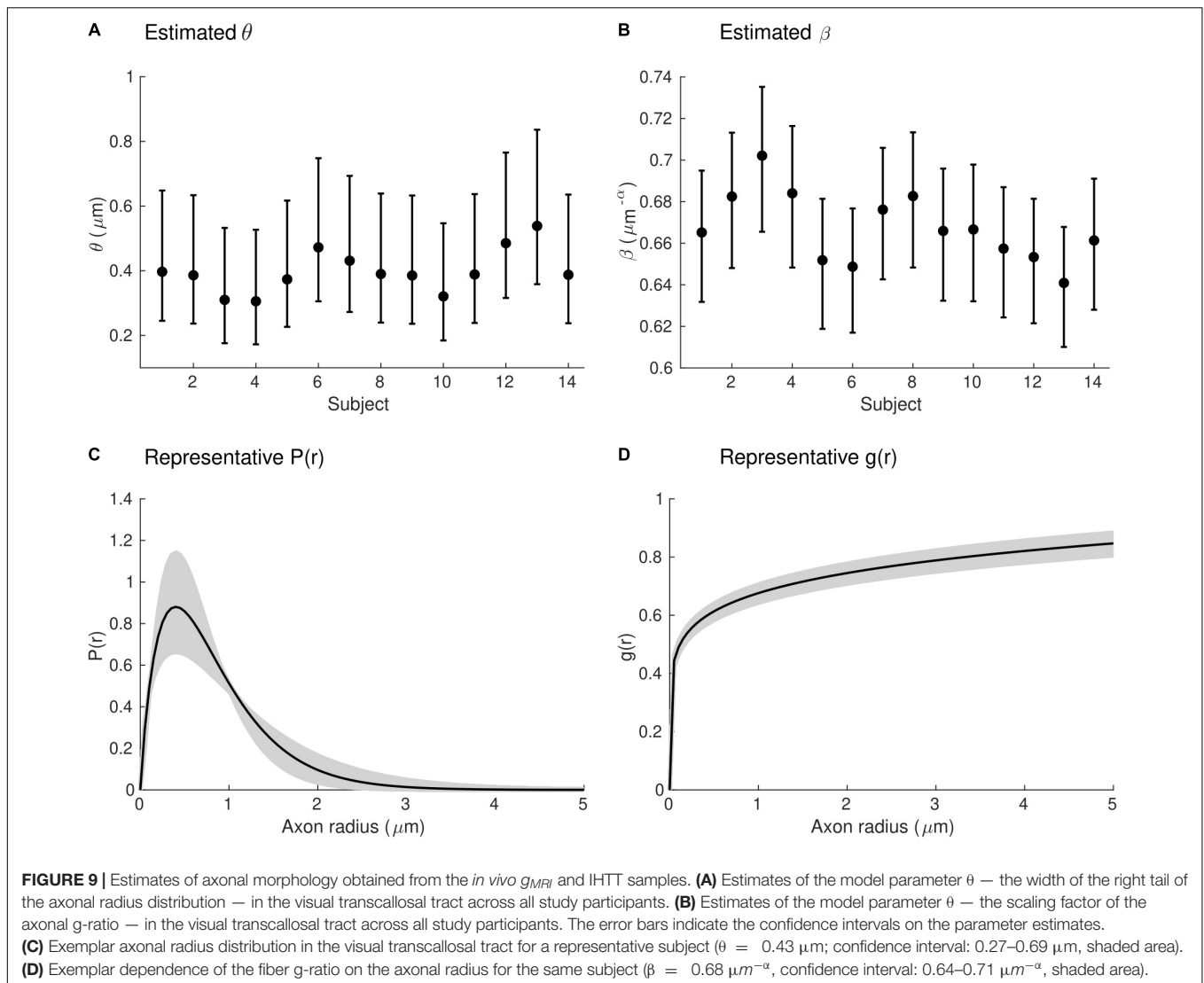
The proposed model is based on the combination of a structural measure of white matter (MRI-measured g-ratio) and a measure of brain function (axonal conduction velocity). The validity of this model relies on the assumption that both measures may be

obtained for a given white matter tract. Anatomical delineation of a white matter tract is generally a routine procedure thanks to MRI tractography techniques (Caminiti et al., 2013; Horowitz et al., 2015; Tournier et al., 2019), allowing the sampling of the MRI-measured g-ratio data along this tract (Schiavi et al., 2022). On the other hand, the underlying mechanisms and anatomy of the inter-hemispheric transfer of the evoked visual activity with Poffenberger's paradigm are still under investigation. Previous literature has used this paradigm to demonstrate an increase in IHTT in acallosal subjects, highlighting the primary role of the CC in visual interhemispheric transfer (Marzi et al., 1991; Di Stefano et al., 1992; Aglioti et al., 1993; Tassinari et al., 1994). In addition, Westerhausen et al. (2006) showed that IHTT is significantly correlated with the structural integrity of the posterior CC, suggesting splenium fibers as the most likely pathway for visual interhemispheric transfer.

The source and target cortical areas of the visual interhemispheric transfer remain to be fully identified. Previous studies have demonstrated the existence of a small patch of transcallosal axons between visual areas 17 and 18 (Clarke and Miklosy, 1990; Aboitiz and Montiel, 2003). This motivated our choice of source and target cortical areas, which led to conduction velocity estimates consistent with previous studies (Caminiti et al., 2013). However, it has been suggested that these connections alone might be insufficient to produce an effective interhemispheric transfer (Innocenti et al., 2015) and higher visual processing areas might be involved.

Future Prospects

The proposed model requires a measure of the MRI-measured g-ratio and axonal conduction velocity in a specific white matter tract of interest. Since measurements of conduction velocity may only be conducted for a limited set of white matter tracts in the human brain, this model, in its current form, cannot be extended to the entire white matter in contrast to other models (e.g., Assaf et al., 2008; Zhang et al., 2011). Instead, this model is geared toward the detailed characterization of a restricted set of white matter tracts. In its proposed form, two parameters relating to the morphology of white matter axons may be estimated from a total of four. Extending the number of estimated parameters requires the use of additional data integrated into the proposed framework. The nature of this data needs to be carefully considered. Alternatively, as was outlined in this work, a subset of the model parameters may be set to a constant value based on histological studies. A prime candidate is the mode of the axonal radius distribution (M), preserved between white matter tracts, individuals, and animal species (Tomasi et al., 2012; Liewald et al., 2014). This choice may need to be reconsidered for the study of brain pathologies that might differentially affect axons of different sizes. Other potential candidates are the parameters α or β that describe the dependence of the fiber g-ratio on axonal radius. In this study, we opted to set α to a constant in expectation of fiber myelination differences identical for all radii. Alternatively, setting β to a constant value may be preferred to allow for the estimation of α , in cases where myelin thickness differences are expected to depend on axonal radius.



In the current study, the estimate of the IHTT was calculated from the average of the EEG-based CD across participants. This led to an average bias in θ and β of 12% and 0.90% across participants, reaching up to 40 and 3%, respectively (Figure 6). While small compared to differences between tracts ($\sim 350\%$ for θ and $\sim 7\%$ for β , see Figure 4), this is of the order of the inter-subject differences for these parameters (Figure 9) and prevents the estimation of axonal morphological features at the individual level. This limitation represents the primary avenue for future improvements. The question of the accuracy of the parameter estimates and their comparison with histological data might arise subsequently. Estimation of the IHTT from alternative techniques such as transcranial magnetic stimulation might also be considered (Lo and Fook-Chong, 2004; Spitzer et al., 2004; Basso et al., 2006; Deftereos et al., 2008; Marzi et al., 2009). We highlight that the parameters of the proposed model touch on properties of brain tissue that have received little attention in histological studies to date. These

include the radius dependence of the axonal g-ratio and the radius dependence of fiber myelination change in health and disease. Validation of the proposed model may therefore bring opportunities for new research avenues for histological studies of the human brain.

CONCLUSION

In summary, we present a novel method that allows the estimation of morphological properties of axons from MRI and EEG data acquired *in vivo* in healthy volunteers. This method enables the combined estimation of axonal radius and myelin thickness and opens the way for improved specificity in studies of the brain conducted from *in vivo* data. The method enables the assessment of the distribution of morphological features across axons and represents a significant step toward *in vivo* histological studies in the human brain.

DATA AVAILABILITY STATEMENT

The datasets presented in this study can be found in online repositories. The names of the repository/repositories and accession number(s) can be found below: doi: 10.5281/zenodo.6027335.

ETHICS STATEMENT

The studies involving human participants were reviewed and approved by Commission d'éthique de la recherche sur l'être humain du canton de Vaud (CER-VD) Avenue de Chailly 23 1012 LAUSANNE Project-ID: 2020-02228. The patients/participants provided their written informed consent to participate in this study.

AUTHOR CONTRIBUTIONS

RO: conception, design of the study, acquisition of MRI and EEG data, data analysis, interpretation, drafting of the manuscript, and critical revision. AP: acquisition of EEG data, data interpretation, and manuscript revision. GD: acquisition of MRI data, data interpretation, and manuscript revision. MDL and AL: conception, design of the study, data interpretation,

drafting of the manuscript, and critical revision. All authors contributed to the article and approved the submitted version.

FUNDING

AL was supported by the Swiss National Science Foundation (grant no 320030_184784) and the ROGER DE SPOELBERCH Foundation. MDL was funded by the University of Lausanne grant "Pro-Femmes" and the Swiss National Science Foundation (grant no CRSK-3_196194).

ACKNOWLEDGMENTS

The MRI data were acquired on the MRI platform of the Clinical Neuroscience Department, Lausanne University Hospital. We are thankful to Ileana Jelescu (Department of Radiology, Lausanne University Hospital) for insightful discussions in the process of writing this manuscript.

SUPPLEMENTARY MATERIAL

The Supplementary Material for this article can be found online at: <https://www.frontiersin.org/articles/10.3389/fnins.2022.874023/full#supplementary-material>

REFERENCES

- Aboitiz, F., and Montiel, J. (2003). One hundred million years of interhemispheric communication: The history of the corpus callosum. *Brazilian J. Med. Biol. Res.* 36, 409–420. doi: 10.1590/S0100-879X2003000400002
- Aboitiz, F., Scheibel, A. B., Fisher, R. S., and Zaidel, E. (1992). Fiber composition of the human corpus callosum. *Brain Res.* 598, 143–153. doi: 10.1016/0006-8993(92)90178-C
- Aglioti, S., Berlucchi, G., Pallini, R., Rossi, G. F., and Tassinari, G. (1993). Hemispheric control of unilateral and bilateral responses to lateralized light stimuli after callosotomy and in callosal agenesis. *Exp. Brain Res.* 95, 151–165. doi: 10.1007/BF00229664
- Alexander, D. C., Hubbard, P. L., Hall, M. G., Moore, E. A., Ptito, M., Parker, G. J. M., et al. (2010). Orientationally invariant indices of axon diameter and density from diffusion MRI. *Neuroimage* 52, 1374–1389. doi: 10.1016/j.neuroimage.2010.05.043
- Andersson, J. L. R., and Sotiropoulos, S. N. (2016). An integrated approach to correction for off-resonance effects and subject movement in diffusion MR imaging. *Neuroimage* 125, 1063–1078. doi: 10.1016/j.neuroimage.2015.10.019
- Assaf, Y., and Basser, P. J. (2005). Composite hindered and restricted model of diffusion (CHARMED) MR imaging of the human brain. *Neuroimage* 27, 48–58. doi: 10.1016/j.neuroimage.2005.03.042
- Assaf, Y., Blumenfeld-Katzir, T., Yovel, Y., and Basser, J. (2008). AxCaliber: A Method for Measuring Axon Diameter Distribution from Diffusion MRI. *Magn. Reson. Med.* 59, 1347–1354. doi: 10.1002/mrm.21577
- Barazany, D., Basser, P. J., and Assaf, Y. (2009). In vivo measurement of axon diameter distribution in the corpus callosum of rat brain. *Brain* 132, 1210–1220. doi: 10.1093/brain/awp042
- Basso, D., Vecchi, T., Kabiri, L. A., Baschenis, I., Boggiani, E., and Bisiacchi, P. S. (2006). Handedness effects on interhemispheric transfer time: A TMS study. *Brain Res. Bull.* 70, 228–232. doi: 10.1016/j.brainresbull.2006.05.009
- Bell, A. J., and Sejnowski, T. J. (1995). An Information-Maximization Approach to Blind Separation and Blind Deconvolution. *Neural Comput.* 7, 1129–1159. doi: 10.1162/neco.1995.7.6.1129
- Burcaw, L. M., Fieremans, E., and Novikov, D. S. (2015). Mesoscopic structure of neuronal tracts from time-dependent diffusion. *Neuroimage* 114, 18–37. doi: 10.1016/j.neuroimage.2015.03.061
- Caminiti, R., Carducci, F., Piervincenzi, C., Battaglia-Mayer, A., Confalone, G., Visco-Comandini, F., et al. (2013). Diameter, length, speed, and conduction delay of callosal axons in macaque monkeys and humans: Comparing data from histology and magnetic resonance imaging diffusion tractography. *J. Neurosci.* 33, 14501–14511. doi: 10.1523/JNEUROSCI.0761-13.2013
- Caminiti, R., Ghaziri, H., Galuske, R., Hof, P. R., and Innocenti, G. M. (2009). Evolution amplified processing with temporally dispersed slow neuronal connectivity in primates. *PNAS* 106, 19551–19556. doi: 10.1073/pnas.0907655106
- Campbell, J. S. W., Leppert, I. R., Narayanan, S., Boudreau, M., Duval, T., Cohen-Adad, J., et al. (2018). Promise and pitfalls of g-ratio estimation with MRI. *Neuroimage* 182, 80–96. doi: 10.1016/j.neuroimage.2017.08.038
- Castella, R., Arn, L., Dupuis, E., Callaghan, M. F., Draganski, B., and Lutti, A. (2018). Controlling motion artefact levels in MR images by suspending data acquisition during periods of head motion. *Magn. Reson. Med.* 80, 2415–2426. doi: 10.1002/mrm.27214
- Chaumillon, R., Blouin, J., and Guillaume, A. (2018). Interhemispheric transfer time asymmetry of visual information depends on eye dominance: An electrophysiological study. *Front. Neurosci.* 12:1–19. doi: 10.3389/fnins.2018.00072
- Clarke, S., and Miklossy, J. (1990). Occipital Cortex in Man: Organization of Callosal Connections, Related Myelo- and Cytoarchitecture, and Putative Boundaries of Functional Visual Areas. *J. Comp. Neurol.* 298, 188–214. doi: 10.1002/cne.902980205
- Cluskey, S., and Ramsden, D. B. (2001). Mechanisms of neurodegeneration in amyotrophic lateral sclerosis. *J. Clin. Pathol. - Mol. Pathol.* 54, 386–392. doi: 10.1136/mp.54.6.386
- Daducci, A., Canales-Rodríguez, E. J., Zhang, H., Dyrby, T. B., Alexander, D. C., and Thiran, J. P. (2015). Accelerated Microstructure Imaging via Convex

- Optimization (AMICO) from diffusion MRI data. *Neuroimage* 105, 32–44. doi: 10.1016/j.neuroimage.2014.10.026
- Deftereos, S. N., Panagopoulos, G., Georgonikou, D., Karageorgiou, E., Andriopoulos, P., and Karageorgiou, C. E. (2008). On the calculation of transcranial conduction time using transcranial magnetic stimulation. *Funct. Neurol.* 23, 137–140.
- Delorme, A., and Makeig, S. (2004). EEGLAB: An open source toolbox for analysis of single-trial EEG dynamics including independent component analysis. *J. Neurosci. Methods* 134, 9–21. doi: 10.1016/j.jneumeth.2003.10.009
- Deslauriers-Gauthier, S., Lina, J. M., Butler, R., Whittingstall, K., Gilbert, G., Bernier, P. M., et al. (2019). White matter information flow mapping from diffusion MRI and EEG. *Neuroimage* 201:116017. doi: 10.1016/j.neuroimage.2019.116017
- Di Russo, F., Martínez, A., Sereno, M. I., Pitzalis, S., and Hillyard, S. A. (2001). Cortical sources of the early components of the visual evoked potential. *Hum. Brain Mapp.* 15, 95–111. doi: 10.1002/hbm.10010
- Di Stefano, M. R., Sauerwein, H. C., and Lassonde, M. (1992). Influence of anatomical factors and spatial compatibility on the stimulus-response relationship in the absence of the corpus callosum. *Neuropsychologia* 30, 177–185. doi: 10.1016/0028-3932(92)90026-I
- Does, M. D. (2018). Inferring Brain Tissue Composition and Microstructure via MR Relaxometry. *Neuroimage* 182, 136–148. doi: 10.1016/j.neuroimage.2017.12.087
- Dortch, R. D., Harkins, K. D., Juttukonda, M. R., Gore, J. C., and Does, M. D. (2013). Characterizing Inter-Compartmental Water Exchange in Myelinated Tissue using Relaxation Exchange Spectroscopy. *Magn. Reson. Med.* 70, 1–20. doi: 10.1002/mrm.24571
- Drakesmith, M., Harms, R., Rudrapatna, S. U., Parker, G. D., Evans, C. J., and Jones, D. K. (2019). Estimating axon conduction velocity in vivo from microstructural MRI. *Neuroimage* 203:116186. doi: 10.1016/j.neuroimage.2019.116186
- Edwards, L. J., Kirilina, E., Mohammadi, S., and Weiskopf, N. (2018). Microstructural imaging of human neocortex in vivo. *Neuroimage* 182, 184–206. doi: 10.1016/j.neuroimage.2018.02.055
- Ellerbrock, I., and Mohammadi, S. (2018). Four in vivo g-ratio-weighted imaging methods: Comparability and repeatability at the group level. *Hum. Brain Mapp.* 39, 24–41. doi: 10.1002/hbm.23858
- Evangelou, N., Konz, D., Esiri, M. M., Smith, S., Palace, J., and Matthews, P. M. (2001). Size-selective neuronal changes in the anterior optic pathways suggest a differential susceptibility to injury in multiple sclerosis. *Brain* 124, 1813–1820. doi: 10.1093/brain/124.9.1813
- Feintuch, A., Zhu, Y., Bishop, J., Davidson, L., Dazai, J., Bruneau, B. G., et al. (2007). 4D cardiac MRI in the mouse. *NMR Biomed.* 20, 360–365. doi: 10.1002/nbm.1164
- Fieremans, E., Jensen, J. H., and Helpert, J. A. (2011). White matter characterization with diffusional kurtosis imaging. *Neuroimage* 58, 177–188. doi: 10.1016/j.neuroimage.2011.06.006
- Fischl, B., Rajendran, N., Busa, E., Augustinack, J., Hinds, O., Yeo, B. T. T., et al. (2008). Cortical folding patterns and predicting cytoarchitecture. *Cereb. Cortex* 18, 1973–1980. doi: 10.1093/cercor/bhm225
- Friedrich, P., Ocklenburg, S., Mochalski, L., Schlüter, C., Güntürkün, O., and Genc, E. (2017). Long-term reliability of the visual EEG Poffenberger paradigm. *Behav. Brain Res.* 330, 85–91. doi: 10.1016/j.bbr.2017.05.019
- Fukunaga, M., Li, T. Q., Van Gelderen, P., De Zwart, J. A., Shmueli, K., Yao, B., et al. (2010). Layer-specific variation of iron content in cerebral cortex as a source of MRI contrast. *Proc. Natl. Acad. Sci. U. S. A.* 107, 3834–3839. doi: 10.1073/pnas.0911177107
- Gibson, E. M., Purger, D., Mount, C. W., Goldstein, A. K., Lin, G. L., Wood, L. S., et al. (2014). Neuronal Activity Promotes Oligodendrogenesis and Adaptive Myelination in the Mammalian Brain. *Science*. 344:1252304. doi: 10.1126/science.1252304
- Gramfort, A., Papadopoulou, T., Olivi, E., and Clerc, M. (2010). OpenMEEG: opensource software for quasistatic bioelectromagnetics. *Biomed. Eng. Online* 9:45. doi: 10.1186/1475-925X-9-45
- Griswold, M. A., Jakob, P. M., Heidemann, R. M., Nittka, M., Jellus, V., Wang, J., et al. (2002). Generalized Autocalibrating Partially Parallel Acquisitions (GRAPPA). *Magn. Reson. Med.* 47, 1202–1210. doi: 10.1002/mrm.10171
- Guerrero, J. M., Adluru, N., Bendlin, B. B., Goldsmith, H. H., Schaefer, S. M., Davidson, R. J., et al. (2019). Optimizing the intrinsic parallel diffusivity in NODDI: An extensive empirical evaluation. *PLoS One* 14:1–17. doi: 10.1371/journal.pone.0217118
- Hämäläinen, M. S., and Ilmoniemi, R. J. (1994). Interpreting magnetic fields of the brain: minimum norm estimates. *Med. Biol. Eng. Comput.* 32, 35–42. doi: 10.1007/BF02512476
- Helbling, S., Teki, S., Callaghan, M. F., Sedley, W., Mohammadi, S., Griffiths, T. D., et al. (2015). Structure predicts function: Combining non-invasive electrophysiology with in-vivo histology. *Neuroimage* 108, 377–385. doi: 10.1016/j.neuroimage.2014.12.030
- Helms, G., Dathe, H., and Dechent, P. (2008a). Quantitative FLASH MRI at 3T using a rational approximation of the Ernst equation. *Magn. Reson. Med.* 59, 667–672. doi: 10.1002/mrm.21542
- Helms, G., Dathe, H., Kallenberg, K., and Dechent, P. (2008b). High-resolution maps of magnetization transfer with inherent correction for RF inhomogeneity and T1 relaxation obtained from 3D FLASH MRI. *Magn. Reson. Med.* 60, 1396–1407. doi: 10.1002/mrm.21732
- Honey, C. J., Thivierge, J. P., and Sporns, O. (2010). Can structure predict function in the human brain? *Neuroimage* 52, 766–776. doi: 10.1016/j.neuroimage.2010.01.071
- Horowitz, A., Barazany, D., Tavor, I., Bernstein, M., Yovel, G., and Assaf, Y. (2015). In vivo correlation between axon diameter and conduction velocity in the human brain. *Brain Struct. Funct.* 220, 1777–1788. doi: 10.1007/s00429-014-0871-0
- Hutton, C., Bork, A., Josephs, O., Deichmann, R., Ashburner, J., and Turner, R. (2002). Image distortion correction in fMRI: A quantitative evaluation. *Neuroimage* 16, 217–240. doi: 10.1006/nimg.2001.1054
- Ikeda, M., and Oka, Y. (2012). The relationship between nerve conduction velocity and fiber morphology during peripheral nerve regeneration. *Brain Behav.* 2, 382–390. doi: 10.1002/brb3.61
- Innocenti, G. M., Caminiti, R., and Aboitiz, F. (2015). Comments on the paper by Horowitz et al. (2014). *Brain Struct. Funct.* 220, 1789–1790. doi: 10.1007/s00429-014-0974-7
- Jelescu, I. O., Palombo, M., Bagnato, F., and Schilling, K. G. (2020). Challenges for biophysical modeling of microstructure. *J. Neurosci. Methods* 344:108861. doi: 10.1016/j.jneumeth.2020.108861
- Jelescu, I. O., Veraart, J., Adisetiyo, V., Milla, S. S., Novikov, D. S., and Fieremans, E. (2015). One diffusion acquisition and different white matter models: How does microstructure change in human early development based on WMTI and NODDI? *Neuroimage* 107, 242–256. doi: 10.1016/j.neuroimage.2014.12.009
- Jenkinson, M., and Smith, S. (2001). A global optimisation method for robust affine registration of brain images. *Med. Image Anal.* 5, 143–156. doi: 10.1016/s1361-8415(01)00036-6
- Jones, D. K., Alexander, D. C., Bowtell, R., Cercignani, M., Dell'Acqua, F., McHugh, D. J., et al. (2018). Microstructural imaging of the human brain with a 'super-scanner': 10 key advantages of ultra-strong gradients for diffusion MRI. *Neuroimage* 182, 8–38. doi: 10.1016/j.neuroimage.2018.05.047
- Jung, W., Lee, J., Shin, H. G., Nam, Y., Zhang, H., Oh, S. H., et al. (2018). Whole brain g-ratio mapping using myelin water imaging (MWI) and neurite orientation dispersion and density imaging (NODDI). *Neuroimage* 182, 379–388. doi: 10.1016/j.neuroimage.2017.09.053
- Kiselev, V. G., and Novikov, D. S. (2018). Transverse NMR relaxation in biological tissues. *Neuroimage* 182, 149–168. doi: 10.1016/j.neuroimage.2018.06.002
- Kybic, J., Clerc, M., Abboud, T., Faugeras, O., Keriven, R., and Papadopoulou, T. (2005). A common formalism for the integral formulations of the forward EEG problem. *IEEE Trans. Med. Imaging* 24, 12–28. doi: 10.1109/TMI.2004.837363
- Lazari, A., and Lipp, I. (2021). Can MRI measure myelin? Systematic review, qualitative assessment, and meta-analysis of studies validating microstructural imaging with myelin histology. *Neuroimage* 230:117744. doi: 10.1016/j.neuroimage.2021.117744
- Lee, H. H., Fieremans, E., and Novikov, D. S. (2018). What dominates the time dependence of diffusion transverse to axons: Intra- or extra-axonal water? *Neuroimage* 182, 500–510. doi: 10.1016/j.neuroimage.2017.12.038

- Liewald, D., Miller, R., Logothetis, N., Wagner, H. J., and Schüz, A. (2014). Distribution of axon diameters in cortical white matter: an electron-microscopic study on three human brains and a macaque. *Biol. Cybern.* 108, 541–557. doi: 10.1007/s00422-014-0626-2
- Lo, Y. L., and Fook-Chong, S. (2004). A transcranial magnetic stimulation study of the ipsilateral silent period in lower limb muscles. *Neurosci. Lett.* 368, 337–340. doi: 10.1016/j.neulet.2004.07.080
- Lutti, A., Corbin, N., Ashburner, J., Ziegler, G., Draganski, B., Phillips, C., et al. (2022). Restoring statistical validity in group analyses of motion-corrupted MRI data. *Hum. Brain Mapp.* 43, 1973–1983. doi: 10.1002/hbm.25767
- Lutti, A., Dick, F., Sereno, M. I., and Weiskopf, N. (2014). NeuroImage Using high-resolution quantitative mapping of R1 as an index of cortical myelination. *Neuroimage* 93, 176–188. doi: 10.1016/j.neuroimage.2013.06.005
- Lutti, A., Hutton, C., Finsterbusch, J., Helms, G., and Weiskopf, N. (2010). Optimization and validation of methods for mapping of the radiofrequency transmit field at 3T. *Magn. Reson. Med.* 64, 229–238. doi: 10.1002/mrm.22421
- Lutti, A., Stadler, J., Josephs, O., Windischberger, C., Speck, O., Bernarding, J., et al. (2012). Robust and fast whole brain mapping of the RF transmit field B1 at 7T. *PLoS One* 7:1–7. doi: 10.1371/journal.pone.0032379
- MacKay, A. L., and Laule, C. (2016). Magnetic Resonance of Myelin Water: An in vivo Marker for Myelin. *Brain Plast.* 2, 71–91. doi: 10.3233/bpl-160033
- Mahjoory, K., Nikulin, V. V., Botrel, L., Linkenkaer-Hansen, K., Fato, M. M., and Haufe, S. (2017). Consistency of EEG source localization and connectivity estimates. *Neuroimage* 152, 590–601. doi: 10.1016/j.neuroimage.2017.02.076
- Marzi, C. A. (1999). The Poffenberger paradigm: A first, simple, behavioural tool to study interhemispheric transmission in humans. *Brain Res. Bull.* 50, 421–422. doi: 10.1016/S0361-9230(99)00174-4
- Marzi, C. A., Bisiacchi, P., and Nicoletti, R. (1991). Is interhemispheric transfer of visuomotor information asymmetric? Evidence from a meta-analysis. *Neuropsychologia* 29, 1163–1177. doi: 10.1016/0028-3932(91)90031-3
- Marzi, C. A., Mancini, F., and Savazzi, S. (2009). Interhemispheric transfer of phosphenes generated by occipital versus parietal transcranial magnetic stimulation. *Exp. Brain Res.* 192, 431–441. doi: 10.1007/s00221-008-1496-4
- Melie-Garcia, L., Slater, D., Ruef, A., Sanabria-Diaz, G., Preisig, M., Kherif, F., et al. (2018). Networks of myelin covariance Lester. *Hum. Brain Mapp.* 39, 1532–1554. doi: 10.1002/hbm.23929
- Miles, W. R. (1930). Ocular dominance in human adults. *J. Gen. Psychol.* 3, 412–430. doi: 10.1080/00221309.1930.9918218
- Mohammadi, S., Carey, D., Dick, F., Diedrichsen, J., Sereno, M. I., Reiser, M., et al. (2015). Whole-brain in-vivo measurements of the axonal G-ratio in a group of 37 healthy volunteers. *Front. Neurosci.* 9:1–13. doi: 10.3389/fnins.2015.00441
- Nilsson, M., Lasič, S., Drobnjak, I., Topgaard, D., and Westin, C. F. (2017). Resolution limit of cylinder diameter estimation by diffusion MRI: The impact of gradient waveform and orientation dispersion. *NMR Biomed.* 30, 1–13. doi: 10.1002/nbm.3711
- Oldfield, R. C. (1971). The assessment and analysis of handedness: the Edinburgh inventory. *Neuropsychologia* 9, 97–113. doi: 10.1016/0028-3932(71)90067-4
- Oostenveld, R., Fries, P., Maris, E., and Schoffelen, J. M. (2011). FieldTrip: Open source software for advanced analysis of MEG, EEG, and invasive electrophysiological data. *Comput. Intell. Neurosci.* 2011:156869. doi: 10.1155/2011/156869
- Plomp, G., Michel, C. M., and Herzog, M. H. (2010). Electrical source dynamics in three functional localizer paradigms. *Neuroimage* 53, 257–267. doi: 10.1016/j.neuroimage.2010.06.037
- Preibisch, C., and Deichmann, R. (2009). Influence of RF spoiling on the stability and accuracy of T1 mapping based on spoiled FLASH with varying flip angles. *Magn. Reson. Med.* 61, 125–135. doi: 10.1002/mrm.21776
- Rushton, W. A. H. (1951). A theory of the effects of fibre size in medullated nerve. *J. Physiol.* 115, 101–122. doi: 10.1113/jphysiol.1951.sp004655
- Saron, C., and Foxe, J. J. (2003). “Complexities of Interhemispheric Communication in Sensorimotor Tasks Revealed by High-Density Event-Related Potential Mapping,” in *The Asymmetrical Brain*, ed. R. J. Eds (Cambridge, MA: MIT press), 342–408. doi: 10.7551/mitpress/1463.003.0014
- Saron, C. D., and Davidson, R. J. (1989). Visual Evoked Potential Measures of Interhemispheric Transfer Time in Humans. *Behav. Neurosci.* 103, 1115–1138. doi: 10.1037/0735-7044.103.5.1115
- Schiavi, S., Lu, P. J., Weigel, M., Lutti, A., Jones, D. K., Kappos, L., et al. (2022). Bundle myelin fraction (BMF) mapping of different white matter connections using microstructure informed tractography. *Neuroimage* 249:118922. doi: 10.1016/j.neuroimage.2022.118922
- Schiffler, P., Tenberge, J.-G., Wiendl, H., and Meuth, S. G. (2017). Cortex Parcellation Associated Whole White Matter Parcellation in Individual Subjects. *Front. Hum. Neurosci.* 11:1–10. doi: 10.3389/fnhum.2017.00352
- Sepehrband, F., Alexander, D. C., Clark, K. A., Kurniawan, N. D., Yang, Z., and Reutens, D. C. (2016). Parametric probability distribution functions for axon diameters of corpus callosum. *Front. Neuroanat.* 10, 1–9. doi: 10.3389/fnana.2016.00059
- Slater, D. A., Melie-Garcia, L., Preisig, M., Kherif, F., Lutti, A., and Draganski, B. (2019). Evolution of white matter tract microstructure across the life span. *Hum. Brain Mapp.* 40, 2252–2268. doi: 10.1002/hbm.24522
- Spitzer, C., Willert, C., Grabe, H. J., Rizos, T., Möller, B., and Freyberger, H. J. (2004). Dissociation, Hemispheric Asymmetry, and Dysfunction of Hemispheric Interaction: A Transcranial Magnetic Stimulation Approach. *J. Neuropsychiatry Clin. Neurosci.* 16, 163–169. doi: 10.1176/jnp.16.2.163
- Stephan, K. E., Tittgemeyer, M., Knösche, T. R., Moran, R. J., and Friston, K. J. (2009). Tractography-based priors for dynamic causal models. *Neuroimage* 47, 1628–1638. doi: 10.1016/j.neuroimage.2009.05.096
- Stikov, N., Campbell, J. S. W., Stroh, T., Lavelée, M., Frey, S., Novek, J., et al. (2015). In vivo histology of the myelin g-ratio with magnetic resonance imaging. *Neuroimage* 118, 397–405. doi: 10.1016/j.neuroimage.2015.05.023
- Stikov, N., Perry, L. M., Mezer, A., Rykhlevskaia, E., Wandell, B. A., Pauly, J. M., et al. (2011). Bound pool fractions complement diffusion measures to describe white matter micro and macrostructure. *Neuroimage* 54, 1112–1121. doi: 10.1016/j.neuroimage.2010.08.068
- Stüber, C., Morawski, M., Schäfer, A., Labadie, C., Wähnert, M., Leuze, C., et al. (2014). Myelin and iron concentration in the human brain: A quantitative study of MRI contrast. *Neuroimage* 93, 95–106. doi: 10.1016/j.neuroimage.2014.02.026
- Sui, J., Huster, R., Yu, Q., Segall, J. M., and Calhoun, V. D. (2014). Function-Structure Associations of the Brain: Evidence from Multimodal Connectivity and Covariance Studies. *Neuroimage* 102, 11–23. doi: 10.1016/j.neuroimage.2013.09.044
- Tabelow, K., Balteau, E., Ashburner, J., Callaghan, M. F., Draganski, B., Helms, G., et al. (2019). hMRI – A toolbox for quantitative MRI in neuroscience and clinical research. *Neuroimage* 194, 191–210. doi: 10.1016/j.neuroimage.2019.01.029
- Tadel, F., Baillet, S., Mosher, J. C., Pantazis, D., and Leahy, R. M. (2011). Brainstorm: A user-friendly application for MEG/EEG analysis. *Comput. Intell. Neurosci.* 2011:879716. doi: 10.1155/2011/879716
- Tassinari, G., Aglioti, S., Pallini, R., Berlucchi, G., and Rossi, G. F. (1994). Interhemispheric integration of simple visuomotor responses in patients with partial callosal defects. *Behav. Brain Res.* 64, 141–149. doi: 10.1016/0166-4328(94)90126-0
- Tomasì, S., Caminiti, R., and Innocenti, G. M. (2012). Areal differences in diameter and length of corticofugal projections. *Cereb. Cortex* 22, 1463–1472. doi: 10.1093/cercor/bhs011
- Tournier, J. D., Smith, R., Raffelt, D., Tabbara, R., Dhollander, T., Pietsch, M., et al. (2019). MRtrix3: A fast, flexible and open software framework for medical image processing and visualisation. *Neuroimage* 202:116137. doi: 10.1016/j.neuroimage.2019.116137
- Veraart, J., Nunes, D., Rudrapatna, U., Fieremans, E., Jones, D. K., Novikov, D. S., et al. (2020). Noninvasive quantification of axon radii using diffusion MRI. *Elife* 9:e49855. doi: 10.7554/eLife.49855
- Waxman, S., and Bennett, M. (1972). Relative Conduction Velocities of Small Myelinated and Non-myelinated Fibres in the Central Nervous System. *Nat. New Biol.* 238, 217–219. doi: 10.1038/newbio238217a0
- Wegiel, J., Kaczmarek, W., Flory, M., Martinez-Cerdeno, V., Wisniewski, T., Nowicki, K., et al. (2018). Deficit of corpus callosum axons, reduced axon diameter and decreased area are markers of abnormal development of interhemispheric connections in autistic subjects. *Acta Neuropathol. Commun.* 6:143. doi: 10.1186/s40478-018-0645-7

- Weiskopf, N., Mohammadi, S., Lutti, A., and Callaghan, M. F. (2015). Advances in MRI-based computational neuroanatomy: From morphometry to in-vivo histology. *Curr. Opin. Neurol.* 28, 313–322. doi: 10.1097/WCO.0000000000000222
- West, K. L., Kelm, N. D., Carson, R. P., and Does, M. D. (2016). A revised model for estimating g-ratio from MRI. *Neuroimage* 125, 1155–1158. doi: 10.1016/j.neuroimage.2015.08.017
- Westerhausen, R., Kreuder, F., Woerner, W., Huster, R. J., Smit, C. M., Schweiger, E., et al. (2006). Interhemispheric transfer time and structural properties of the corpus callosum. *Neurosci. Lett.* 409, 140–145. doi: 10.1016/j.neulet.2006.09.028
- Whitford, T. J., Kubicki, M., Ghorashi, S., Hawley, K. J., and McCarley, R. W. (2011). Predicting Inter-Hemispheric Transfer Time from the Diffusion Properties of the Corpus Callosum in Healthy Individuals and Schizophrenia Patients: A Combined ERP and DTI Study. *Neuroimage* 54, 2318–2329. doi: 10.1016/j.neuroimage.2010.10.048
- Zhang, H., Hubbard, P. L., Parker, G. J. M., and Alexander, D. C. (2011). Axon diameter mapping in the presence of orientation dispersion with diffusion MRI. *Neuroimage* 56, 1301–1315. doi: 10.1016/j.neuroimage.2011.01.084
- Zhang, H., Schneider, T., Wheeler-kingshott, C. A., and Alexander, D. C. (2012). NODDI: Practical in vivo neurite orientation dispersion and density imaging of the human brain. *Neuroimage* 61, 1000–1016. doi: 10.1016/j.neuroimage.2012.03.072
- Conflict of Interest:** The authors declare that the research was conducted in the absence of any commercial or financial relationships that could be construed as a potential conflict of interest.
- Publisher's Note:** All claims expressed in this article are solely those of the authors and do not necessarily represent those of their affiliated organizations, or those of the publisher, the editors and the reviewers. Any product that may be evaluated in this article, or claim that may be made by its manufacturer, is not guaranteed or endorsed by the publisher.

Copyright © 2022 Oliveira, Pelentritou, Di Domenicantonio, De Lucia and Lutti. This is an open-access article distributed under the terms of the Creative Commons Attribution License (CC BY). The use, distribution or reproduction in other forums is permitted, provided the original author(s) and the copyright owner(s) are credited and that the original publication in this journal is cited, in accordance with accepted academic practice. No use, distribution or reproduction is permitted which does not comply with these terms.